

Doping superlattices in conventional and wide-bandgap semiconductors: Physics, properties, and device applications

Xiao-Long Wu(武小龙), Geng-You Zhao(赵耕右), Bo Feng(冯博), Han-Ming Ding(丁汉明), Liang-Xue Gu(顾梁雪), Chuang Wang(王闯), Cheng Wang(王成), Kun Tang(汤琨), Shu-Ming Zhu(朱顺明), Jian-Dong Ye(叶建东), Shu-Lin Gu(顾书林)

Citation: Chin. Phys. B. 35, 097301 (2026). DOI: 10.1088/1674-1056/ae6d9a | CSTR: 32038.14.CPB.ae6d9a
http://cpb.iphy.ac.cn; http://iopscience.iop.org/cpb

What follows is a list of articles you may be interested in

Short-wavelength infrared InAs/GaSb superlattice hole avalanche photodiode

Jia-Feng Liu(刘家丰), Ning-Tao Zhang(张宁涛), Yan Teng(滕奘), Xiu-Jun Hao(郝修军), Yu Zhao(赵宇), Ying Chen(陈影), He Zhu(朱赫), Hong Zhu(朱虹), Qi-Hua Wu(吴启花), Xin Li(李欣), Bai-Le Chen(陈佰乐), Yong Huang(黄勇)
Chin. Phys. B. 29, 117301 (2020). DOI: 10.1088/1674-1056/aba2e0

Electronic properties of silicene in BN/silicene van der Waals heterostructures

Ze-Bin Wu(吴泽宾), Yu-Yang Zhang(张余洋), Geng Li(李更), Shixuan Du(杜世萱), Hong-Jun Gao(高鸿钧)
Chin. Phys. B. 27, 077302 (2018). DOI: 10.1088/1674-1056/27/7/077302

Modulation of electronic properties with external fields in silicene-based nanostructures

Li Geng(李庚), Zhao Yin-Chang(赵银昌), Zheng Rui(郑蕊), Ni Jun(倪军), Wu Yan-Ning(吴言宁)
Chin. Phys. B. 24, 087302 (2015). DOI: 10.1088/1674-1056/24/8/087302

Synthesis and electrical properties of $In_2O_3(ZnO)_m$ superlattice nanobelt

Tang Xin-Yue(唐欣月), Gao Hong(高红), Wu Li-Li(武立立), Wen Jing(温静), Pan Si-Ming(潘思明), Liu Xin(刘欣), Zhang Xi-Tian(张喜田)
Chin. Phys. B. 24, 027305 (2015). DOI: 10.1088/1674-1056/24/2/027305

Dependence of electron dynamics on magnetic fields in semiconductor superlattices

Yang Gui(杨癸), Wang Lei(王磊), Tian Jun-Long(田俊龙)
Chin. Phys. B. 22, 127305 (2013). DOI: 10.1088/1674-1056/22/12/127305

REVIEW

Doping superlattices in conventional and wide-bandgap semiconductors: Physics, properties, and device applications

Xiao-Long Wu(武小龙), Geng-You Zhao(赵耕右), Bo Feng(冯博), Han-Ming Ding(丁汉明), Liang-Xue Gu(顾梁雪), Chuang Wang(王闯), Cheng Wang(王成), Kun Tang(汤琨), Shu-Ming Zhu(朱顺明), Jian-Dong Ye(叶建东), and Shu-Lin Gu(顾书林)[†]

School of Electronic Science & Engineering, Nanjing University, Nanjing 210023, *China*

(Received 23 March 2026; revised manuscript received 10 May 2026; accepted manuscript online 14 May 2026)

Doping superlattices (DSLs) provide a multifunctional platform for engineering carrier distribution and band structure in semiconductors. In this work, we present a comprehensive review of the physical mechanisms and device applications of DSLs in both conventional III–V and wide-bandgap semiconductor systems. Based on a self-consistent Schr"odinger–Poisson framework within the local density approximation, the formation of subband structures, effective bandgap modulation, and spatial separation of carriers are systematically analyzed. The tunable optoelectronic properties of DSLs are discussed under optical excitation, electrical injection, and external fields, including conductivity, absorption, refractive index, and luminescence. Typical device implementations such as solar cells, photodetectors, electro-optic modulators, and negative-differential-resistance devices are reviewed, with emphasis on the interplay between internal electric fields and carrier recombination dynamics. Furthermore, recent progress in extending DSL concepts to wide-bandgap semiconductors is summarized. In AlGaN, polarization-assisted modulation doping effectively enhances hole activation and transport, while in diamond, δ-doping and p–i–p–i structures offer a potential route toward high-mobility two-dimensional hole gases. Finally, the feasibility of n–i–n–i superlattice architectures for improving n-type doping in diamond is discussed. These results highlight DSL engineering as a general strategy for tunable and high-performance semiconductor devices.

Keywords: doping superlattices, band structure engineering, wide-bandgap semiconductors, diamond

PACS: 73.21.–b, 71.20.–b, 71.20.Nr, 81.05.ug

DOI: 10.1088/1674-1056/ae6d9a **CSTR:** 32038.14.CPB.ae6d9a

1. Introduction

With the rapid development of modern electronic and optoelectronic technologies, the demand for semiconductor materials with enhanced performance is steadily increasing, particularly in high-power, high-frequency, and deep-ultraviolet applications.[1–3] Doping superlattices (DSLs), as a novel class of semiconductor structures, have become an important area of research due to their unique ability to regulate carrier behavior and their tunable band structure.[4,5] By precisely controlling the thickness, concentration, and distribution of doped layers, DSL structures allow for the spatial separation of carriers, significantly improving carrier mobility, carrier lifetime, and optoelectronic properties.[4,6,7]

DSLs can be designed in various structural forms depending on the specific application requirements, including n–i–p–i, n–p–n–p, n–i–n–i, p–i–p–i, and heterojunction n–i–p–i structures. Each structure has its own distinct characteristics and advantages:

n–i–p–i structure This structure is widely used in optoelectronic devices, particularly in light conversion and radiation hardness applications.[8–12] By inserting an intrinsic (i-type) layer between the n-type and p-type materials, carrier isolation is effectively achieved, enhancing the photoresponse speed and extending carrier lifetime. However, the relatively thick intrinsic layer can reduce carrier transport efficiency, particularly in high-power or high-frequency applications.

n–p–n–p structure Compared to the n–i–p–i structure, the n–p–n–p structure offers enhanced carrier injection and faster response speeds, making it suitable for high-frequency and high-power optoelectronic devices.[13] However, the complexity of the structure and the dense doping layers increase manufacturing costs and technical difficulty.

n–i–n–i and p–i–p–i structures These single-polarity doping superlattices (n–i–n–i and p–i–p–i) are typically used to address the challenges of p-type doping in wide-bandgap semiconductors. Due to their relatively weaker modulation potentials, these structures do not exhibit the same significant advantages in carrier separation and carrier lifetime as bipolar doping superlattices like the n–i–p–i structure.[14] Nevertheless, these structures are widely used in p-type modulation doping in AlGaN and δ-doping in diamond, particularly in improving the performance of deep-ultraviolet AlGaN optoelectronic devices and enhancing the high-speed performance of diamond field-effect transistors (FETs).[7,15,16]

Heterojunction n–i–p–i structure The heterojunction

[†]Corresponding author. E-mail: slgu@nju.edu.cn

© 2026 Chinese Physical Society and IOP Publishing Ltd. All rights, including for text and data mining, AI training, and similar technologies, are reserved.

n–i–p–i structure enhances device performance by forming heterojunctions between different materials. Compared to homojunction structures, heterojunctions can better exploit the material property differences, improving light conversion efficiency and overall device performance.[17–21] However, the drawbacks of heterojunctions lie in the difficulty of controlling interface quality, and the difference in thermal expansion coefficients between materials may induce stress and defects, affecting long-term device stability.

By carefully designing and optimizing different types of doping superlattice structures, researchers can achieve optimal performance for specific applications. This review will focus on the applications of doping superlattices in III-V semiconductor materials, particularly the n–i–p–i structure. The n–i–p–i superlattice has demonstrated excellent performance in light conversion, optoelectronic detection, and optical modulation, making it widely applicable in solar cells, photodetectors, and optical modulators. Furthermore, this review will explore the application of doping superlattices in wide-bandgap semiconductor materials (such as AlGaN and diamond), particularly the latest research advances in p-type doping and carrier mobility enhancement.

Through a comprehensive review of recent experimental and theoretical studies, this article aims to provide an in-depth overview of the applications of doping superlattices in semiconductor devices and look forward to their potential development in next-generation high-performance optoelectronic devices.

2. Theoretical foundations of doping superlattices

Accurately describing the electronic structure of n–i–p–i crystals requires a rigorous theoretical framework, which is typically established on the basis of self-consistent methods within the local density approximation (LDA). The overall computational flow is schematically illustrated in Fig. 1. For the initial ground-state calculation, a simplifying assumption is usually made: only shallow donors and acceptors are present, and the crystal is in a macro-compensated state, meaning that all impurities are assumed to be completely ionized.

The electronic states are determined by solving the Schrödinger equation within a local density functional formalism combined with the effective-mass approximation[22]

$$\left[-\frac{\hbar^2}{2m_{\mathrm{e}}}\nabla^2+v_0(z)+v_{\mathrm{H}}(z)+v_{xc}(z)\right]\psi_{\mu\boldsymbol{k}}(\boldsymbol{r}) = \varepsilon_{\mu k}\psi_{\mu k}(\boldsymbol{r}). \tag{1}$$

Considering the inherent periodicity of the potential energy along the growth direction z and its invariance with respect to the in-plane coordinates x and y, Eq. (1) can be transformed into

$$\left[-\left(\frac{\hbar^2}{2m_{\mathrm{e}}}\right)\left(\frac{\partial^2}{\partial z^2}\right)+v_0(z)+v_H(z)+v_{xc}(z)\right]\xi_{\mu k_z}(z) = \varepsilon*\mu k_z\xi_{\mu k_z}(z), \tag{2}$$

where $\hbar$ is the reduced Planck constant, m_{e} is the effective mass of the electron. $v_0(z)$ is the bare superlattice potential, which is directly generated by the periodic distribution of ionized impurities; $v_H(z)$ represents the Hartree potential, which is the classical electrostatic potential generated by the distribution of free electrons inside the superlattice; $v_{xc}(z)$ represents the exchange-correlation potential, which is actually a quantum mechanical correction term derived under the framework of the local density approximation (LDA). $\psi_{\mu\boldsymbol{k}}(\boldsymbol{r})$ is the wave function, $\xi_{\mu k_z}(z)$ is the superlattice Bloch function corresponding to the subband μ and wave vector k_z. $\varepsilon_{\mu k_z}$ is the energy eigenvalue corresponding to the subband μ and wave vector k_z.

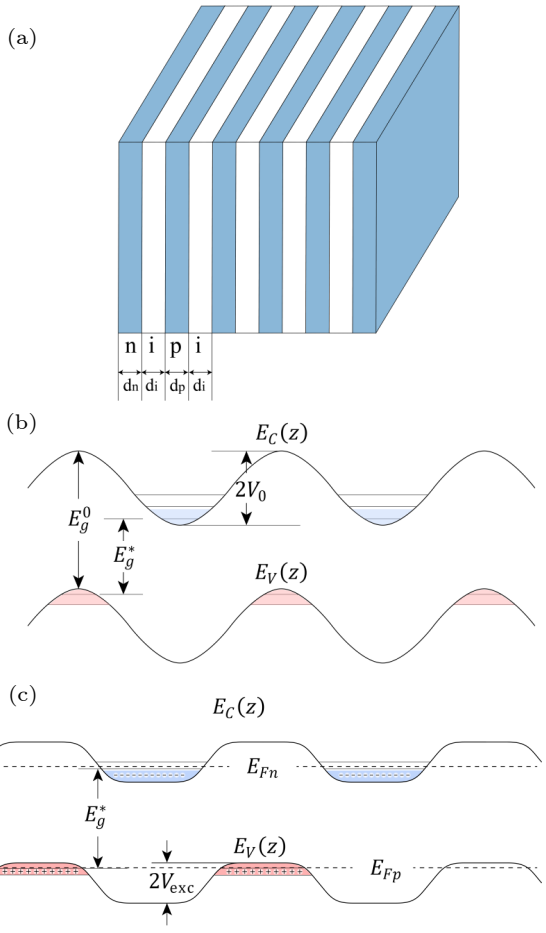


Fig. 1. Schematic illustration and corresponding energy band diagrams of an n–i–p–i doping superlattice.[4] The periodic stacking of n-, i-, and p-type layers (a) gives rise to a spatially modulated electrostatic potential from ionized impurities, which in turn induces a periodic modulation of the conduction and valence band edges, $E_{\mathrm{C}}(z)$ and $E_{\mathrm{V}}(z)$, as shown in panel (b). The spatial separation of electrons and holes across the potential barriers leads to a reduced and tunable effective bandgap E_{g}^*. Under carrier excitation (c), quasi-Fermi levels E_{Fn} and E_{Fp} are established, and the shaded regions denote potential barriers that suppress electron–hole recombination. The arrows indicate the tunneling and thermally activated recombination pathways.

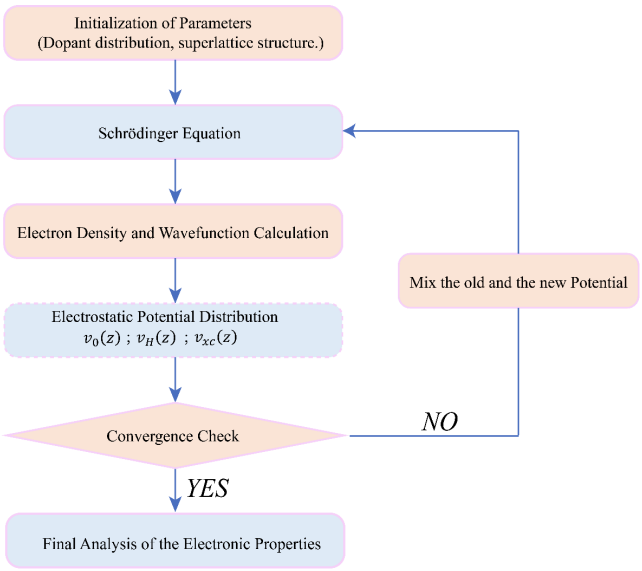


Fig. 2. Computational workflow for the electronic structure of doped superlattices.

From the Schr"odinger equation, one can calculate the eigenstates (or subband wavefunctions) under given boundary conditions, and thereby obtain the carrier distribution or electron density. Following the approach pioneered by Döhler,[2] the potential distribution inside the superlattice can be evaluated using Poisson's equation in conjunction with the local density approximation (LDA), enabling the next iteration of the self-consistent loop (Fig. 2). As depicted in Fig. 1, convergence of the electron density and potential energy is used as the criterion for self-consistency, ensuring that the obtained solution corresponds to a stable and physically realistic state.

Although this theoretical model exhibits high reliability, it inherently depends on a number of simplifying assumptions. Ruden and Döhler[2] carefully examined the effects of these approximations. The model neglects spatial potential fluctuations arising from the random distribution of impurities and the discrete point-charge nature of dopants, which could otherwise lead to impurity-bound states or impurity bands. Döhler argued that, for practical GaAs-based doping superlattice devices, a small number of free electrons or holes can compensate a certain amount of space charge, thereby suppressing long-range potential fluctuations. Moreover, the unscreened Coulomb energy associated with impurity point charges is sufficiently small, leading to negligible shifts in subband energies; thus, short-range potential fluctuations can also be ignored.

Within both the tight-binding and nearly-free-electron approximations, the formation of donor impurity bands can be safely neglected. However, for acceptors, the situation differs: due to the significantly larger heavy-hole effective mass (m_{h}^{*}), typically several times that of the electron effective mass, the corresponding Bohr radius $\left(a_{\mathrm{A}}^{\mathrm{h}} \approx 1.8\ \mathrm{nm}\right)$ is much smaller.[22] Under the tight-binding approximation, the hole occupation of the valence-band states effectively neutralizes the negatively charged acceptor ions. In such cases, the standard self-consistent calculation becomes invalid, and the central region of the p-type layer (with a width proportional to the hole concentration, denoted as $\left(d_{p0} = p^{(2)}/n_{\mathrm{A}}\right)$) is usually treated as a neutral region.[4] Nevertheless, experimental studies on the photoluminescence spectra of GaAs doping superlattices have shown that the observed linewidths are significantly broader than those predicted theoretically, indicating that impurity-induced spatial potential fluctuations in the excited-state system can no longer be neglected. To address this discrepancy, the modified Kane model was employed, providing improved agreement between theory and experiment.[23]

The doping concentration and period thickness of the n–i–p–i doped superlattice can modulate the ground-state band structure, as shown in the basic formula below:

$$2V_0 = \frac{2\pi e^2}{\kappa_0}\left[n_{\mathrm{D}}\left(\frac{d_{\mathrm{n}}}{2}\right)^2 + n_{\mathrm{A}}\left(\frac{d_{\mathrm{p}}}{2}\right)^2\right].$$

For gallium arsenide materials, when $n_{\mathrm{D}} = n_{\mathrm{A}} \geq 3 \times 10^{18}\ \mathrm{cm}^{-3}$, tunneling recombination dominates at room temperature, and the bandgap is adjustable; below this value, thermally activated recombination dominates, and the bandgap is not adjustable. Through the above theoretical framework, the concept of two-dimensional subband structure in superlattices naturally arises. This subband configuration evidently varies with carrier concentration, leading to corresponding variations in the effective bandgap $\left(E_{\mathrm{g}}^{*}\right)$ and the subband spacings. The tunable physical properties of doping superlattices fundamentally originate from these features — what Döhler referred to as their "tunability".

In addition, the spatial separation of electrons and holes in such structures gives rise to exceptionally long minority-carrier lifetimes. Döhler[24] analyzed the enhancement factors of carrier lifetime resulting from both tunneling and thermally activated processes, elucidating their dependence on carrier concentration and effective lifetime.

3. Modulation of doping superlattice properties

As discussed above, the tunable characteristics of doping superlattices arise primarily from the modulation of internal carrier concentrations. The main modulation mechanisms include optical injection and electrical injection, while additional control can be achieved through external transverse electric fields or in-plane magnetic fields, which modify the optoelectronic behavior of the system. The effects of these modulation schemes typically manifest as tunable electron and hole conductivities, adjustable absorption coefficients, refractive indices, optical nonlinearities, and tunable spontaneous and stimulated emission spectra. This section provides a review of these properties.

3.1. External modulation in doping superlattices

The tunable properties of doping superlattices primarily arise from the modulation of carrier concentrations within the structure. These superlattices exhibit distinct optoelectronic behaviors that can be controlled by external factors such as optical injection, electrical bias, and transverse electric or magnetic fields (Fig. 3). This section provides an overview of the key physical characteristics and the mechanisms by which these properties are controlled.

(i) Optical injection When doping superlattices absorb photons with energy greater than the effective bandgap, electron–hole pairs are generated (Figs. 3(a) and 3(d)). Due to the spatial separation of carriers in the superlattice, recombination is significantly delayed, allowing photogenerated carriers to accumulate effectively in the n-type and p-type layers. This long-lived carrier separation makes DSLs ideal for applications in photonic memory and light-controlled switching, where sustained carrier concentration is required.[4]

(ii) Electrical injection Electrical injection in DSLs utilizes selective contacts to the n-type and p-type layers, enabling direct control of the quasi-Fermi levels of the electrons and holes (Figs. 3(b) and 3(e)). By applying a bias, carriers are injected or extracted, with the quasi-Fermi level difference modulated by the external voltage. Electrical modulation results in faster response times compared to optical modulation, as the process is governed primarily by the RC time constant rather than recombination dynamics.

(iii) Transverse electric field modulation A transverse electric field applied perpendicular to the superlattice layers superimposes a linear potential term on the intrinsic periodic potential, altering the symmetry of the potential wells (Figs. 3(c) and 3(f)). This results in spatially varying bandgaps, with some regions experiencing an increase in bandgap (blue-shift) and others experiencing a decrease (red-shift). This spatial variation in the bandgap modulates carrier recombination lifetimes and offers ultrafast tunability.

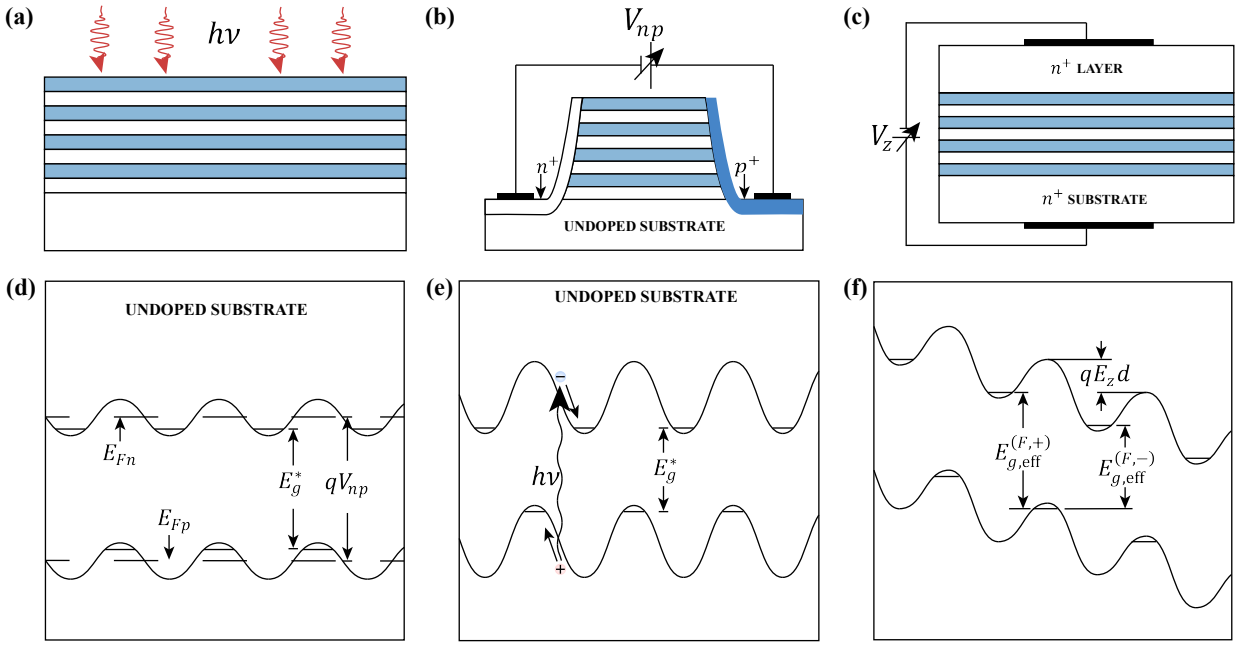


Fig. 3. Optical and electrical modulation of an n–i–p–i crystal.[4] (a) Optical excitation by incident photons. (b) Carrier injection or extraction through selective n- and p-type contacts under applied bias. (c) Electrical modulation by an external field normal to the layers. (d)–(f) Corresponding band diagrams illustrating quasi-Fermi-level separation, optical excitation across the effective bandgap, and field-induced bandgap modulation.

3.2. Modulation of electron and hole conductivity

The spatial separation of electrons and holes in n–i–p–i structures results in bipolar conductivity, which can be modulated through either selective electrical contacts or optical injection. The term "bipolar-junction field-effect transistor" was coined by Ploog *et al.*[25] to describe the independent modulation of n- and p-channel conductivity in n–i–p–i structures. Unlike conventional JFETs or BJTs, this architecture lacks a physical gate electrode; instead, conductivity is controlled via selective optical or electrical injection into alternating layers.

Although this specific device architecture did not gain widespread follow-up, it provided experimental confirmation of the dual-component conductivity in n–i–p–i systems, expressed as

$$\sigma = q\left(\mu_{\mathrm{n}} n_{2\mathrm{D}} + \mu_{\mathrm{p}} p_{2\mathrm{D}}\right)/d, \tag{3}$$

where q is the elementary charge, μ_{n} and μ_{p} are the carrier mobilities in the n- and p-type layers, $n_{2\mathrm{D}}$ and $p_{2\mathrm{D}}$ denote the two-dimensional carrier concentrations in the respective layers, and d is the superlattice period. This equation explicitly relates the 2D carrier concentrations to the quasi-Fermi-level

separation, revealing that the total conductivity can be externally modulated by electric fields.

As discussed earlier, the extremely long recombination lifetime of excess carriers in n–i–p–i doping superlattices results in exceptionally high photoconductive gain. For instance, a GaAs n–i–p–i mesa structure operated at room temperature with a 1 V bias and a 0.45 mm contact spacing exhibits a photoconductive gain g exceeding 10^3, far surpassing that of bulk GaAs (limited to $g \approx 10$–20 due to hole sweep-out effects).[4]

Furthermore, Künzel *et al.*[26] performed Hall-effect measurements at 4.2 K on molecular-beam-epitaxy (MBE)-grown GaAs periodic p–n doping superlattices. They showed that the in-plane conductivity arises from both carrier concentration and mobility contributions, with mobility enhancement attributed to the screening of space-charge potentials by photogenerated carriers, which broadens the homogeneous conduction regions. Similar phenomena have also been observed in wide-bandgap semiconductors, as will be discussed in Section 5.

3.3. Modulation of optical properties

(i) Modulation of the absorption coefficient Because of the existence of an effective bandgap E_g^*, photons with energies exceeding E_g^* can be absorbed in doping superlattices. Moreover, the Franz–Keldysh effect (FKE) induced by internal space-charge fields allows for the absorption of lower-energy photons, resulting in a sub-bandgap absorption tail that has been experimentally observed in large-period doping superlattices.[27]

For highly doped, small-period superlattices ($d_n = d_p =$ 20 nm, $N_D = 10^{18}$ cm^{-3}), the presence of 2D subbands introduces pronounced step-like structures in the absorption coefficient ($\alpha(V)$) even below the host bandgap.[28] Under electrical bias, the subband structure collapses as the bias transitions from low forward to near-threshold reverse voltages, leading to a distinct absorption tail. This substantially reduces the recombination current and produces large relative variations in absorption $\alpha(V)$, demonstrating strong tunability.[27,28] The usual expression for $\alpha(V)$ is

$$\alpha^{\mathrm{nipi}}\left(\omega;\Delta\phi_{\mathrm{np}}\right) \approx d^{-1}\int_0^d \mathrm{d}z\alpha_{\mathrm{bulk}}\left(\omega;F_i\left(z\right)\right), \tag{4}$$

where $F_i(z)$ is the built-in electric field.[27]

Experimental studies have demonstrated substantial modulation of the absorption coefficient. Hasnain *et al.*[29] reported that, for a 1.95 μm-thick GaAs n–i–p–i sample under bias from −0.5 V to +0.5 V, the transmittance change near 0.89 μm wavelength reached 9%, while at photon energies 180 meV below the bulk bandgap, the absorption coefficient varied by over a factor of 30 for a 0.65 V bias change. Gulden *et al.*[30] confirmed that in $In_{0.07}Ga_{0.93}As$/GaAs hetero-n–i–p–i structures, the combined influence of band-filling and FKE leads to enhanced absorption modulation. Applying biases from −2.5 V to +0.8 V produced absorption changes exceeding 2000 cm^{-1} at 1.39 eV, far exceeding the prediction of FKE alone (≈ 1450 cm^{-1}). The transmission variation exceeded 100% within a 26 meV range, demonstrating high spectral stability against temperature and wavelength detuning.

By applying time-varying electric fields to highly doped, small-period superlattices, high-frequency modulation of optical transmission can be achieved. Layers where the effective bandgap is smaller than the photon energy exhibit large relative changes in absorption, making them suitable for high-extinction-ratio optical modulators. In hetero-n–i–p–i structures resembling modulation-doped systems, the absorption edges and step structures become sharper, enhancing the selectivity for photons corresponding to distinct subband transitions.

(ii) Refractive index and nonlinear optical properties As mentioned earlier, both electrical and optical modulation can alter the absorption coefficient; consequently, doping superlattices exhibit pronounced nonlinear optical behavior. In general, the nonlinearities in n–i–p–i and hetero-n–i–p–i structures arise primarily from band-filling, free-carrier polarization, and the Franz–Keldysh effect.[4,31]

The extraordinarily long carrier recombination lifetime enables strong optical nonlinearities even under low excitation intensities, and the superposition of band-filling and field effects can lead to constructive enhancement. Malzer *et al.*[31] found that in hetero-n–i–p–i structures, the energy difference between the intrinsic and doped layers can align the field-induced absorption tail with the doped-layer bandgap, resulting in a switching enhancement factor of approximately 4500 cm^{-1}. Since changes in the absorption coefficient $\Delta\alpha$ correspond to variations in the refractive index n, the latter can be evaluated using the Kramers–Kronig transformation

$$\Delta n_{\mathrm{opt}}\left(\omega\right) = \frac{\hbar c}{\pi}\int_0^x \Delta\alpha\left(\omega'\right)\left[\omega'^2-\omega^2\right]^{-1}\mathrm{d}\omega'. \tag{5}$$

For high-frequency optical modulation, combining optical injection with selective electrical contacts allows the absorption switching time constant to be controlled to the nanosecond level via external bias tuning.

(iii) Modulation of luminescence characteristics Due to the coexistence of the effective and direct bandgaps (E_g^* and E_g), n–i–p–i structures exhibit two primary radiative recombination channels: tunable recombination across the spatial indirect gap (dominant at low temperatures) and thermally activated vertical recombination (dominant at high temperatures, near the bulk gap).[32]

Heitzer *et al.*[33] theoretically analyzed the emission, absorption, and optical gain spectra of n–i–p–i structures under various temperatures, excitation levels, and design parameters, with excellent agreement with experimental results. At 77 K,

multiple small peaks corresponding to specific subband transitions appear in the emission spectra, while at room temperature, high-energy state occupation leads to smooth broadening and the emergence of a "shoulder" near the bulk band edge due to thermally activated transitions. Experimental and theoretical studies have demonstrated that heavily doped GaAs superlattices exhibit tunable luminescence at room temperature under both optical and electrical injection. Heitzer *et al.* reported that in a GaAs n–i–p–i device containing ten n-type and eleven p-type layers with $Al_{0.3}Ga_{0.7}As$ cladding, an optimized design yielded a tunability of approximately 0.6 eV, consistent with theoretical predictions.

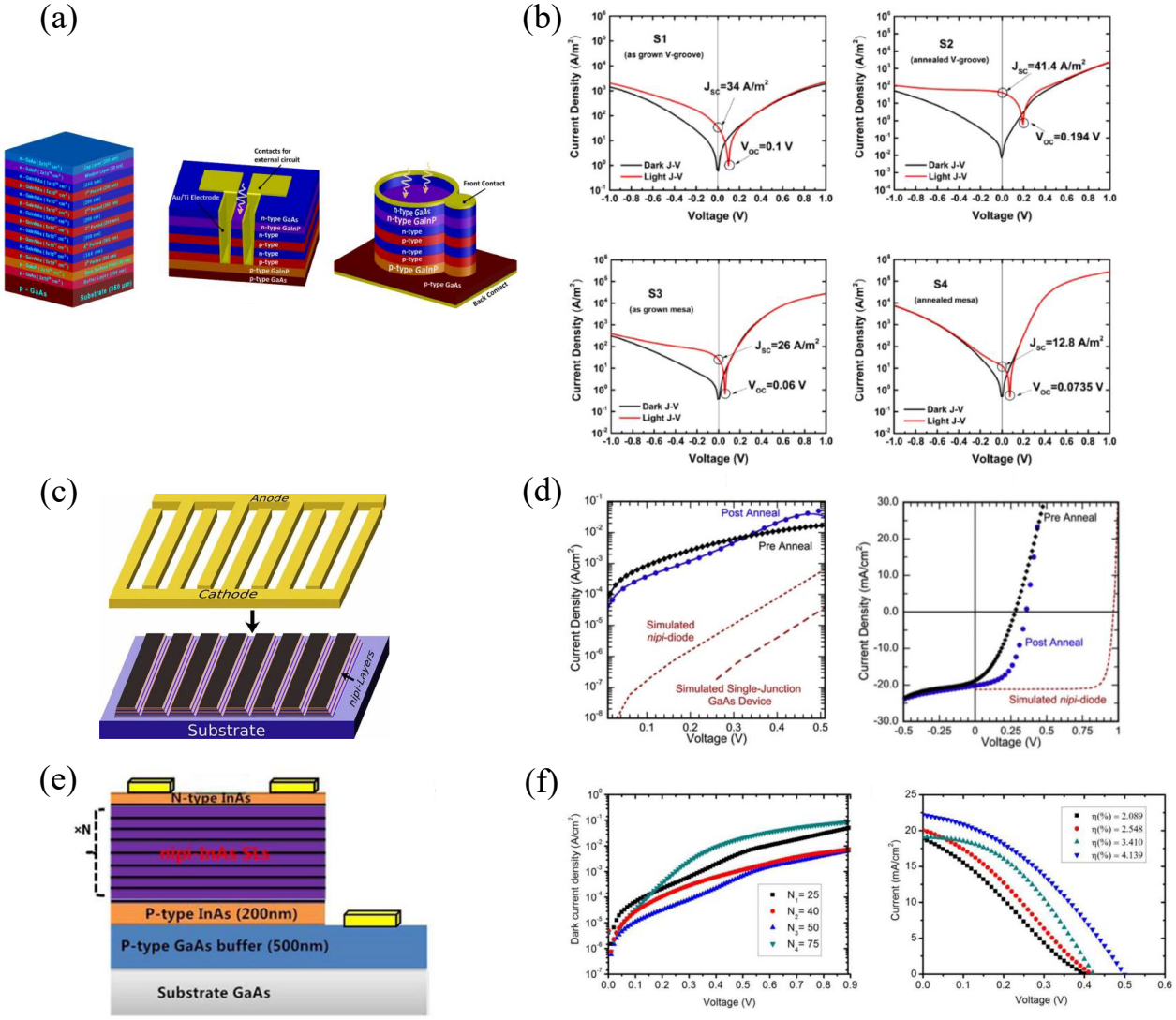


Fig. 4. Structural schematics and electrical characteristics of n–i–p–i superlattice devices. (a) Schematic diagrams of GaInNAs n–i–p–i structures with V-groove and mesa metallization designs. (b) Dark and illuminated *J*–*V* curves of GaInNAs n–i–p–i solar cells before and after annealing.[10] (c) Interdigitated electrode configuration on V-groove mesa n–i–p–i structures. (d) Simulated and measured *J*–*V* characteristics of n–i–p–i diodes before and after contact annealing.[35] (e) Cross-sectional view of an InAs/GaAs n–i–p–i heterostructure. (f) *J*–*V* and open-circuit voltage characteristics of n–i–p–i solar cells with different period numbers.[8]

Although the recombination lifetime in n–i–p–i crystals is substantially prolonged, efficient real-space indirect electron–hole recombination can still produce high emission intensities when the lifetime enhancement is properly controlled by the doping level. Moreover, the emission strength scales with the ratio of carrier density to recombination lifetime; even with strong redshift, the emission strength remains high, since recombination occurs throughout a thick, engineered n–i–p–i volume rather than a confined quantum well. Lateral-field modulation can achieve faster response times but introduces bandgap splitting, yielding simultaneous red- and blue-shifted components. This issue can be mitigated through asymmetric doping profiles or hetero-n–i–p–i architectures.[36] Finally, n–i–p–i systems display remarkable potential for stimulated emission. Compared to conventional semiconductor lasers, population inversion can be achieved at substantially lower injection levels, owing to the extended recombination lifetime. Even at low excitation, the electron quasi-Fermi level in the conduction subbands can exceed k_BT at room temperature, while high p-type doping ensures that the hole quasi-Fermi

level resides within a region of large density of p-states.

The optical gain spectra of n–i–p–i crystals are highly tunable because the gain peak correlates directly with the adjustable effective bandgap. In GaAs-based n–i–p–i structures, gain peaks of the order of 10^3 cm^{-1} have been measured approximately 150 meV below the GaAs bandgap, shifting toward higher photon energies with increasing excitation.[34] Because the absorption losses — arising mainly from free-carrier and inter-valence-band absorption — are relatively small, and Auger recombination is strongly suppressed due to reduced wavefunction overlap, n–i–p–i crystals can achieve extremely low threshold currents. Consequently, the tunable gain characteristics make n–i–p–i crystals highly promising candidates for tunable lasers and optical amplifiers.[4]

4. Research progress on doping superlattice devices

4.1. Optoelectronic devices

(i) Solar cells Compared to conventional p–n junction solar cells, DSL-based photovoltaic devices offer two distinct advantages. First, the tunable effective bandgap allows the absorption spectrum to be extended into the sub-bandgap region of the host material, enabling a multi-spectral response without the need for complex multi-junction growth. Second, the spatial separation of photogenerated carriers within the n- and p-doped layers significantly suppresses bulk recombination. This increases the minority carrier lifetime and enhances the collection efficiency of photogenerated pairs, potentially leading to higher open-circuit voltages and improved conversion efficiencies in materials with low diffusion lengths (Fig. 4).

Subsequent theoretical simulations optimized structural parameters — including the number of periods, layer thickness, and doping concentration — and revealed that increasing the period number improves the short-circuit current density (J_{sc}) but reduces the open-circuit voltage (V_{oc}) (Fig. 4(e)).[8] Cress *et al.*[34] fabricated a three-period GaAs n–i–p–i solar cell consisting of 200–1000 nm doped layers and 200 nm intrinsic spacers (Fig. 4(d)). After post-growth annealing, its performance improved markedly: V_{oc} rose from 0.28 V to 0.36 V, J_{sc} from 19.3 mA/cm^2 to 20.7 mA/cm^2, and the fill factor (FF) from 36% to 53%, yielding an AM0 efficiency of 3.17%. A 12-period device (50 nm per layer, 2.55 μm total thickness) reached 3.42% efficiency with $V_{oc} = 0.643$ V and $J_{sc} = 16.2$ mA/cm^2.[37] Mazzucato *et al.*[41] fabricated triple-junction GaAs n–i–p–i devices (300–1000 nm active region) yielding $J_{sc} = 16$ mA/cm^2, $V_{oc} = 0.33$ V, FF = 54%, and 2.2% efficiency (AM1.5G). Agageldi Muhammetgulyyev *et al.*[10] reported a five-period GaInNAs device whose annealed V-groove structure achieved $J_{sc} = 19$ mA/cm^2, $V_{oc} = 0.21$ V, F = 42%, and 1.69% efficiency. Further interface-optimization work by Slocum *et al.*[38,44] reduced trap density and boosted efficiency to 9.14%, while maintaining nearly 100% of J_{sc}, V_{oc}, FF, and efficiency after 1 MeV electron irradiation (Fig. 5).

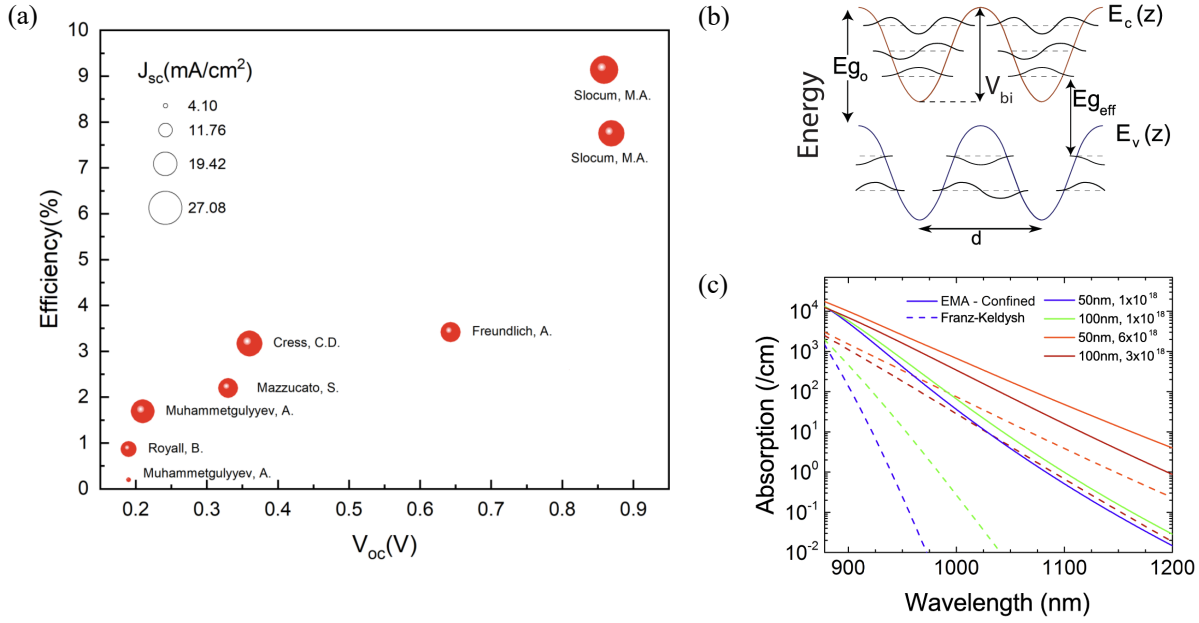


Fig. 5. Performance and physical mechanisms of GaAs doped superlattice solar cells.[8–10,34,37–43]

Figure 6 illustrates the impact of doping superlattice or δ-doped structures on both the electrical and optical properties of optoelectronic devices.[8–10,34,37–43] As shown in Fig. 6(a), the device efficiency exhibits a non-monotonic dependence on V_{oc}. While increasing V_{oc} generally benefits efficiency, the maximum short-circuit current density J_{sc} occurs at relatively low V_{oc}, indicating a trade-off between carrier collection and built-in potential. This reflects the interplay between inter-

nal electric fields and recombination: enhanced band bending improves carrier separation and V_{oc}, but may degrade carrier transport and increase recombination, thereby reducing J_{sc}.

Figures 6(b) and 6(c) further demonstrate enhanced long-wavelength absorption arising from the Franz–Keldysh effect under strong internal fields.[43] In Fig. 6(c), the absorption spectrum shows a clear redshift and an extended tail toward longer wavelengths, indicating sub-bandgap absorption. The Franz–Keldysh model yields a smoother absorption edge than the effective mass approximation, consistent with field-assisted tunneling across the reduced bandgap. Moreover, structural parameters, including layer thickness and doping concentration, strongly influence the absorption strength and spectral range. Overall, DSL structures enable field-induced bandgap modulation and sub-bandgap absorption, while device performance is ultimately limited by the trade-off between V_{oc} and J_{sc}.

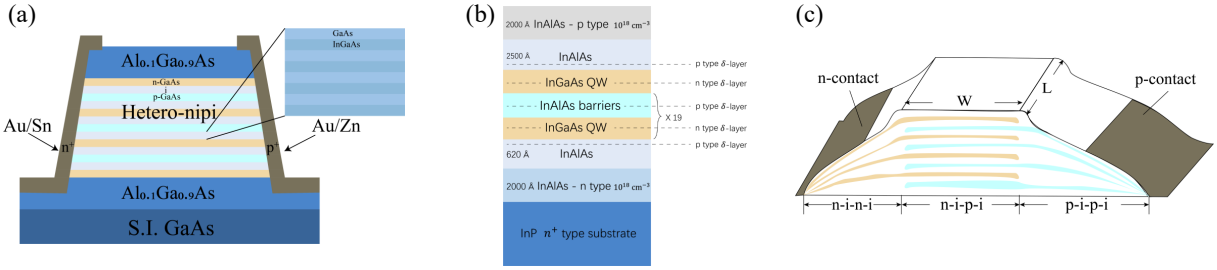


Fig. 6. Device structures and schematic diagrams for multi-quantum well (MQW) light modulators with delta-doping superlattices.[19,45,46] (a) End view of the waveguide device structure for an implanted sample in a light modulator. (b) Scheme of the InGaAs/InAlAs MQW structure with the n–i–p–i delta-doping superlattice for a light modulator. (c) Schematic picture of the sample structure with n–i–n–i, n–i–p–i, and p–i–p–i regions for light modulation.

In Fig. 5(f), the structure and optoelectronic performance of InAs doping superlattice solar cells are closely correlated.[8] Research indicates that the photoelectric conversion efficiency reaches a peak value of 4.14% when the number of superlattice periods is 50, with efficiency following a trend of increasing and then decreasing as the number of periods rises. Regarding layer thickness and doping, a repeating period thickness of 50 nm combined with a doping concentration of 1×10^{18} cm^{-3} generates an internal maximum built-in electric field exceeding 3.6×10^{5} V/cm, which drives the rapid collection of photogenerated carriers. Significant trade-offs exist between device performance indicators. First, while increasing the number of periods enhances the short-circuit current density to 19.06 mA/cm^2 by expanding the absorption volume, it also introduces more parallel junctions and increases the cumulative depletion region thickness, leading to a concurrent rise in dark current. When the number of periods is excessive (e.g., 75 periods), increased lattice strain and defects cause dark current to deteriorate significantly, undermining efficiency. Second, the expansion of the spectral response range comes at the cost of open-circuit voltage (V_{oc}). Although the n–i–p–i structure extends the absorption edge to 1050 nm and improves external quantum efficiency (EQE) in the 900–1000 nm range, the open-circuit voltage drops from 1.05 V for a typical GaAs single-junction cell to approximately 0.4 V due to interface traps and high dark current. Furthermore, while the strong built-in electric field enhances subband absorption via the Franz–Keldysh effect, it simultaneously weakens exciton resonance effects within the semiconductor; the total subband absorption is thus limited by the mutual constraints of these mechanisms. Therefore, optimizing such cells requires finding a balance between the number of periods, the electric field strength induced by doping levels, and the suppression of dark current and voltage loss.

(ii) Photodetectors Unlike conventional homojunction or heterojunction photodetectors, DSL-based structures offer a tunable effective bandgap mechanism. By adjusting the doping concentrations and layer thicknesses, the absorption edge can be extended far into the infrared region, which is otherwise inaccessible for the bulk material. Furthermore, the spatial separation of electrons and holes in DSLs significantly suppresses the recombination rate, thereby enhancing the carrier lifetime and improving the internal quantum efficiency, especially under low-light conditions. Doping-superlattice infrared detectors have evolved through diverse material systems and architectures — including In(As,Sb) sawtooth doping superlattices (SDS), InSb/InAs n–i–p–i structures, and trapezoidal δ-doped superlattices — to achieve mid- and long-wavelength infrared (LWIR, 8–12 μm and beyond) detection.[11,13,47,48] Using MBE growth, researchers achieved high doping densities ($\sim10^{19}$ cm^{-3}) and precise period control (<300 Å),[12] thereby optimizing the absorption coefficient, detectivity (D), and gain–bandwidth product.[12,48] These III–V superlattices offer superior uniformity and thermal stability compared with conventional HgCdTe (CMT), providing a practical route for large-format focal-plane arrays.

Hass *et al.*[13] designed an $InAs_{0.4}Sb_{0.6}$ SDS with $<4\times10^{12}$ cm^{-2} sheet doping and <300 Å period, achieving a cutoff wavelength $\lambda_{(c)}>12$ μm at 77 K. Trapezoidal δ-doped superlattices based on InSb, InAs, GaAs, and Ge ex-

hibit sub-bandgap absorption under high fields, maintaining $\alpha_{\text{eff}} \approx 10^2$ cm^{-1} at 10 μm for InSb.[47] Vaghjiani *et al.*[11] observed strong 10 μm subband absorption with full width at half maximum (FWHM) ≈ 390 cm^{-1} ($\Delta\lambda/\lambda \approx 29\%$). Riel *et al.*[49] and other groups[50] developed reverse-biased photoconductive detectors (RBPCDs) with gain–bandwidth products > 20 GHz, operating efficiently up to 6 GHz for high-bit-rate receivers and optical switches. Although further improvement in substrate quality and integration is required, these efforts demonstrate the feasibility of multi-material and multi-architecture approaches to replace CMT in spaceborne sensing, imaging, and optical-communication applications.

4.2. Electro-optic devices

In optical communication, DSL-based modulators provide a superior alternative to conventional bulk or quantum-well structures due to their enhanced electro-absorption and electro-refraction effects. By applying a transverse or longitudinal electric field, the overlap between electron and hole wavefunctions can be rapidly modulated, leading to a significant shift in the absorption edge and refractive index at much lower driving voltages. This enhanced Franz–Keldysh effect in DSLs enables high-speed modulation with high contrast ratios and lower power consumption, making them ideal for integrated photonic circuits.

Early work focused on electro-optic devices containing n–i–p–i active layers, sawtooth superlattices, or modulation-doped multiple quantum wells (MQWs). Ackley *et al.*[51] demonstrated GaAs LEDs with ten periods of alternating n-type (Si: 3×10^{18} cm^{-3}) and p-type (Be: 3×10^{18} cm^{-3}) layers, each ≈ 300 Å thick. The devices showed a reverse breakdown voltage > 9.5 V and reverse saturation current ≈ 8.8 nA for 400 μm length. Sawtooth superlattice LEDs—comprising alternating δ-doped n and p GaAs layers (20 spikes, sheet density 5×10^{12} cm^{-2}, 10 nm spacing)—emitted quasi-monochromatic light ($\lambda \geq 0.9$ μm) with FWHM $\approx$ 60 meV (41 nm linewidth) and linear intensity–current dependence up to 1 kA·cm^{-2}.[52]

Modulation-doped InGaAsP quantum-well lasers showed α-factors of 1.0–1.4, threshold currents ≈ 20 mA, and output powers ≈ 1.2 mW.[20,21] Schubert *et al.*[53] reported a GaAs sawtooth superlattice laser with 20 nm period, sheet density 5×10^{12} cm^{-2}, and active region thickness 0.2 μm; under 750 ns pulsed excitation at room temperature, the threshold current density was 2.2 kA·cm^{-2} and emission at 905 nm (FWHM ≈ 7.3 meV). Photopumped GaAs doping superlattice lasers with 10 periods (120 Å n$^+$/120 Å p$^+$, 2×10^{18} cm^{-3}) produced continuous-wave and pulsed emission up to 901.5 nm, confirming stimulated emission in DSL media.[54] These devices achieve spectral extension ($\lambda \geq$ 0.9 μm) and surface-emission capabilities, while modulation-doped InGaAsP QW lasers enable low-noise, wide-bandwidth operation around 1.55 μm. Despite remaining challenges such as thermal degradation and complex growth processes, these studies laid the foundation for modern telecommunication-grade light sources. The study by Dutta *et al.* demonstrates that increasing the p-type doping concentration leads to a significant optimization in device performance.[20] When the concentration exceeds 10^{18} cm^{-3}, the relaxation oscillation frequency can be enhanced by more than twofold compared to undoped devices, accompanied by a rapid reduction in the linewidth enhancement factor and the suppression of relative intensity noise.

4.3. Transistors

The primary advantage of integrating GaAs doping superlattices into transistors is the transition from a simple current-control device to a functional integrated component with non-linear logic. By utilizing artificial bandgap engineering, the SDS structure induces a controllable S-shaped negative-differential-resistance (NDR) effect, granting the transistor unique logic switching and bi-stable memory capabilities.[55,56] Liu *et al.* fabricated homojunction and heterojunction BJTs with five-period $\delta(n^+)$–i–$\delta(p^+)$–i collectors ($\delta = 1 \times 10^{13}$ cm^{-2}, 300 Å intrinsic spacers). The homojunction device achieved a common-emitter gain ≈ 20 and base sensitivity $\left(S_B = 8 \times 10^{-3}\ \text{V}/\mu\text{A}\right)$, while the heterojunction variant showed gain ≈ 25 and $\left(S_B = 1.6 \times 10^{-1}\ \text{V}/\mu\text{A}\right)$. δ-Doped InGaAs/GaAs interband tunneling diodes exhibited N-type NDR with peak-to-valley current ratio (PVCR) ≈ 5 and peak current density ≈ 607 A·cm^{-2}; δ-SBITDs achieved PVCR ≈ 3.2, outperforming InSb counterparts.[57] In p-GaAs/SDS/n$^+$-GaAs structures with five $\delta(n^+)$–i–$\delta(p^+)$–i periods, S-type NDR appeared at 77 K due to avalanche multiplication within the SDS region, while room-temperature behavior was dominated by thermionic emission.[58] These results shed light on carrier-transport mechanisms in δ- and SDS structures and suggest their utility for switching and multi-valued logic circuits, though most demonstrations remain at low temperatures and require further optimization for room-temperature operation.

In SDS transistors, the non-linear transport characteristics are highly dependent on structural parameters. First, the sharpness of the δ- doping profile determines the barrier height and carrier confinement depth, which is essential for maintaining low leakage current in the "off-state". As the number of superlattice periods increases, the impact ionization path is extended and hole accumulation is enhanced, significantly improving the switching voltage ratio (V_S/V_H). This hole accumulation creates a charge-screening effect that lowers the internal barrier, triggering a transition from a high-resistance state to a conducting state, which results in the characteris-

tic S-shaped NDR. Furthermore, through optimized layer sequencing, the base current can sensitively control the barrier lowering in the collector, allowing the device to achieve controllable switching functionality alongside traditional transistor amplification. The core of further optimizing GaAs SDS transistors lies in the precise management of charge feedback dynamics. By reducing the intrinsic layer thickness to introduce quantum tunneling, the carrier transit speed across the barrier can be increased, significantly shortening the NDR switching time.

4.4. Optical modulators

(1) Electro-optic modulators Compared to bulk-material electro-optic modulators, DSL structures exhibit significantly enhanced electro-absorption and electro-refraction effects (such as the enhanced Franz–Keldysh effect). Due to the high sensitivity of the periodic potential to external fields, a relatively small bias voltage can cause a substantial shift in the overlap integral of electron and hole wavefunctions. This allows for high-contrast optical modulation with much lower driving voltages, meeting the requirements of high-speed and low-power consumption for integrated photonic circuits. During the 1990s, significant effort was devoted to semiconductor electro-optic modulators based on n–i–p–i superlattices and MQW heterostructures, utilizing the Franz–Keldysh effect (FKE) and quantum-confined Stark effect (QCSE) for electroabsorption control. Kiesel *et al.*[59] fabricated a GaAs n–i–p–i modulator (15 periods, 60 nm n/p layers, 70 nm intrinsic layer, total thickness 3.9 μm). With a 7 V drive swing and no cavity enhancement, an on/off ratio $> 6:1$ and absorption change > 2000 cm^{-1} were achieved; 45×45 μm^2 devices reached 3 dB bandwidths of 40 MHz.

Further studies focused on MQW hetero-n–i–p–i waveguide modulators. Knupfer *et al.*[45] and Thirstrup *et al.*[60] designed structures where each period comprised n-, intrinsic (MQW), and p-regions with doping around 10^{18} cm^{-3}. The former achieved 32 dB extinction at 1.06 μm and 5 V bias with −3 dB bandwidth up to 110 MHz, while the latter demonstrated $>$ 100:1 extinction at 4 V bias under low optical power ($\sim 10^{-5}$ W). Larsson *et al.*[61,62] realized δ-doped InGaAs/GaAs MQW cavities (2.04 μm total thickness) with contrast ratio $>$ 60:1, insertion loss 4.6 dB, and $\Delta\alpha \approx 9000$ cm^{-1}. Yoffe *et al.*[63] achieved 10:1 modulation ratio at only 1 V bias. Tribuzy *et al.*[64] fabricated InP/InGaAsP/InP p–i–n modulators with $\Delta\alpha_{\max} \approx 3000$ cm^{-1} for fields $< 2 \times 10^5$ V·cm^{-1}. Although issues such as insertion loss and doping control persist, these studies demonstrated feasible routes to high-speed, low-voltage optical modulation.

Further, Tribuzy's group systematically investigated n–i–p–i δ-doped MQWs grown by MOVPE in GaAs/AlGaAs and InGaAs/InAlAs systems, with δ- doping levels $\sim 1 \times 10^{12}$ cm^{-2}. In GaAs/AlGaAs structures, electroabsorption enhancement by a factor of three over undoped samples was observed at $\Delta E = 74$ kV·cm^{-1}.[17] Stark shift doubled, and the operating voltage for CR = 14 dB dropped from 3.7 V to 2.0 V.[18] The chirp parameter (α_1) was maintained within the ideal range ($-1 < \alpha_1 < 0$) for long-distance optical communications.[65] In InGaAs/InAlGaAs MQWs, $\Delta\alpha$ improved fourfold under 40 kV·cm^{-1} field, $CR = 15$ dB with 40% lower drive voltage, along with polarization insensitivity and negative chirp.[19]

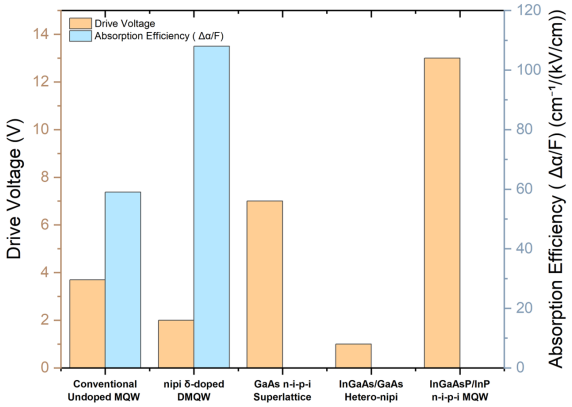


Fig. 7. Performance comparison of n–i–p–i δ-doped DMQW and conventional MQW modulators.[17,18,59,63,66]

The performance enhancement of GaAs-based doping superlattice optical modulators relies on the precise regulation of internal electric field profiles and carrier dynamics. By evolving traditional homogeneous doping into asymmetric δ-doping profiles — specifically, hetero-n–i–p–i structures where n-type δ-layers are positioned at the center of quantum wells and p-type δ-layers at the center of barriers — it is possible to utilize highly localized charge distributions to generate steep sawtooth potential fields. This configuration establishes a strong initial internal electric field at zero bias, maintaining the energy bands in a pre-bent state. Consequently, a relatively low external bias can induce significant band-flattening shifts. This process substantially improves the efficiency of the QCSE, directly optimizing the correlation between driving voltage and absorption coefficient changes, which allows the device to achieve high-contrast optical modulation under low-voltage conditions. In the path toward performance optimization, suppressing the thermal diffusion of dopants (such as C or Be) is critical for maintaining ideal potential field symmetry, as charge compensation or positional deviation at interfaces can lead to distortions in the internal electric field distribution, thereby weakening modulation efficiency. Regarding the inherent intrinsic capacitance of the superlattice, the core of optimization lies in adjusting the ratio between the number of periods and the intrinsic layer thickness to reduce the RC time constant and enhance response bandwidth while ensuring sufficient optical interaction length (Fig. 7).

(2) Bistable and nonlinear optical devices In the realm of nonlinear optics, the core advantage of DSLs is their 'giant" nonlinear coefficients, which are typically several orders of magnitude larger than those of conventional bulk semiconductors. This extreme nonlinearity arises from the high sensitivity of the subband structure to the density of optically injected carriers; the flattening of the potential barriers directly modulates the optical response functions of the material. Such a unique mechanism enables optical bistability at ultra-low power thresholds, providing an ideal platform for all-optical switching and signal processing. Research has also explored bistability and nonlinear optical behavior in n–i–p–i and p–i–n structures at ultra-low optical power. Kiesel *et al.*[67] demonstrated 'intelligent pixel" devices combining n–i–p–i modulators with optical–electrical bistability: with input powers < 200 pW, an electrical current switching ratio $> 10^7$ and optoelectronic gain of 6.8×10^6 were achieved. Opto–optical bistable pixels exhibited optical gain $\approx 3 \times 10^5$, switching power < 500 pW, and hysteresis width ≈ 200 pW, tunable via reference-light bias. Riel *et al.*[49] developed eight-layer p-i-n-i-p or n–i–p–i structures showing electrical bistability with gains $\sim 10^3$, conductance modulation from nS to mS at sub-pW power levels, limited primarily by reverse dark current.

These innovations — leveraging spatial separation of absorption and detection zones — enable ultra-high gain, low-power, and broadband optical switching. While early devices were constrained by slow dynamic response, ongoing research combining heterostructure engineering and advanced doping control continues to push bistable and nonlinear n–i–p–i devices toward practical integration.

5. δ-doping and doping superlattices in wide-bandgap semiconductors

While DSLs in conventional III–V semiconductors are primarily utilized to modulate effective bandgaps and enhance optoelectronic nonlinearities in the infrared and visible spectra, their application in wide-bandgap (WBG) systems addresses a fundamentally different and critical challenge: the severe bottleneck of inefficient doping. As device applications extend into the deep-ultraviolet region and high-power electronics, WBG materials such as AlGaN and diamond suffer from deep impurity levels and extremely low room-temperature activation efficiencies.[68] The DSL architecture provides an innovative solution to bypass these fundamental thermodynamic limits.

5.1. Modulation doping in AlGaN superlattices

Aluminum gallium nitride (AlGaN), as an important member of the ultra-wide bandgap semiconductor family, exhibits great potential in optoelectronic and microelectronic applications owing to its tunable bandgap (ranging from $\sim$ 3.4 eV for GaN to $\sim$ 6.2 eV for AlN), high critical breakdown field, high saturation electron drift velocity, and excellent thermal conductivity and chemical stability.[1,2] However, compared with the relatively mature n-type doping techniques, p-type doping in AlGaN remains a formidable challenge, which has severely limited the improvement of device performance and the expansion of application fields.[1,2] Achieving efficient and stable p-type AlGaN has become one of the key bottlenecks in advancing III-nitride semiconductor technology. Magnesium (Mg) is currently recognized as the most prominent p-type dopant for both AlGaN and GaN materials.[1,69] The ionization energy (or activation energy) of Mg acceptors in AlGaN is relatively large — typically on the order of several hundred millielectronvolts — and increases further with higher Al composition, due to the upward shift of the valence band maximum. As a result, the hole concentration drops sharply with increasing Al content. Moreover, the limited solubility of Mg in AlGaN and the formation of Mg–H complexes can further neutralize the doping effect. Consequently, p-type AlGaN typically exhibits high resistivity, low hole concentration, and poor hole mobility, which together hinder the realization of high-performance electronic and optoelectronic devices. To overcome these inherent difficulties associated with conventional bulk p-type doping, researchers have drawn inspiration from the successful application of modulation doping techniques in other semiconductor systems (such as GaAs/AlGaAs heterostructures) and have begun exploring their applicability in AlGaN-based materials.[70,71]

This chapter summarizes recent advances in p-type modulation doping within AlGaN/GaN superlattices, focusing on the mechanisms, experimental progress, and challenges associated with improving hole concentration, mobility, and conductivity.

5.1.1. p-type modulation doping in AlGaN/GaN superlattices

AlGaN/GaN superlattices have become an important platform for achieving efficient p-type doping due to their unique capability for band structure engineering and polarization control. In such structures, Mg dopants are selectively introduced into the AlGaN barrier layers, while the GaN well layers remain undoped or lightly doped. The fundamental physical mechanism relies on the bandgap difference between AlGaN and GaN and the spontaneous and piezoelectric polarization effects inherent to III-nitride materials, which together produce band bending at the heterointerface favorable for hole accumulation and transport.[72–76,86]

One of the most critical advantages of this superlattice design is its ability to effectively mitigate the long-standing problem of the high activation energy of Mg acceptors in wide-bandgap nitrides. In conventional bulk AlGaN, the deep

Mg acceptor level (typically 250–350 meV above the valence band maximum) limits hole generation at room temperature. However, in the AlGaN/GaN superlattice configuration, the strong polarization-induced electric fields at the heterointerfaces cause significant valence-band bending, forming a potential well for holes in the GaN well layer (Fig. 8). This polarization field effectively lowers the relative energy difference between the Mg acceptor level in the AlGaN barrier and the valence band edge in the GaN well, thereby reducing the effective activation energy for Mg ionization. As a result, holes ionized from Mg acceptors are efficiently transferred into the GaN quantum wells, where the band alignment and internal fields stabilize them, leading to a higher active hole concentration.[75–80,86,87] Moreover, because the Mg ions remain spatially separated in the AlGaN barriers, impurity scattering in the GaN wells is greatly suppressed, enhancing hole mobility and improving overall conductivity.[81–84,88–91]

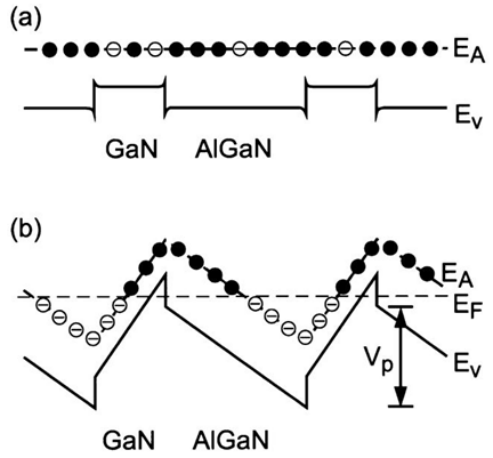


Fig. 8. Schematic illustration of the valence band shape for AlGaN/GaN SLs.[72] (a) Without taking the strain effect into account, (b) with the strain effect taken into account.

Theoretical calculations have strongly supported the feasibility of p-type modulation doping in AlGaN/GaN heterostructures.[6,15,16,74,93–98] Schubert *et al.*[71] demonstrated, both theoretically and experimentally, that AlGaN/GaN superlattices exhibit efficient p-type doping with reduced acceptor activation energies and improved conductivity. Hackenbuchner *et al.*[96] further revealed that spontaneous and piezoelectric polarization can significantly enhance hole concentrations. Hsu *et al.*[16] predicted that strain-induced polarization fields can dramatically facilitate the transfer of holes from the relatively deep Mg acceptor levels in AlGaN barriers to the GaN wells, resulting in a two-dimensional hole gas (2DHG) with sheet densities exceeding 10^{12} cm^{-2} and low-temperature mobilities surpassing 10^4 cm$^2 \cdot$V$^{-1} \cdot$s^{-1}. These findings point to the enormous potential of p-type modulation-doped AlGaN/GaN superlattices as high-mobility p-channel materials.

Early experimental investigations have verified these theoretical predictions.[72,76,86,91] For instance, Kumakura *et al.*[72] reported that in an $Al_{0.15}Ga_{0.85}N$/GaN superlattice with a period of 360 Å (240 Å/120 Å), the sheet hole concentration reached 8×10^{12} cm^{-2} (corresponding to a bulk concentration of 3×10^{18} cm^{-3}), confirming that a strain-induced piezoelectric field ($\sim$ 1 MV/cm) tilted the valence band, lowered the acceptor level below the Fermi level, and facilitated the transfer of holes from Mg acceptors in AlGaN barriers to GaN wells, thus enhancing acceptor activation. Subsequent studies analyzed how parameters such as superlattice period thickness, Al composition, doping configuration (e.g., δ-doping or barrier-layer doping), strain engineering (e.g., insertion of AlN interlayers), and polarization fields influence the resulting hole concentration, resistivity, and mobility. For example, Zheng *et al.*[91] demonstrated that a multidimensional Mg-doped superlattice could achieve a hole concentration of 3.5×10^{18} cm^{-3} and a resistivity of 0.7 $\Omega \cdot$cm, representing several tens of times improvement over conventional superlattice structures. Secondary ion mass spectrometry (SIMS) confirmed Mg accumulation near heterointerfaces with comparable Mg–H ratios to traditional structures, indicating effective activation. Atomic force microscopy (AFM) further revealed pronounced surface steps favorable for vertical hole transport. Similarly, Chen *et al.*[86] observed an effective hole mobility of 36.1 cm$^2 \cdot$V$^{-1} \cdot$s^{-1}, representing a 4.57$\times$ improvement compared with uniformly doped counterparts.

5.1.2. Applications of p-type modulation-doped AlGaN

The advancement of p-type modulation-doped AlGaN has provided new insights into overcoming the long-standing challenge of achieving p-type conduction in III-nitride semiconductor devices, with promising implications for several key application areas.[99–118]

One of the most direct and important applications is in deep-ultraviolet (DUV) optoelectronic devices, particularly DUV LEDs (Fig. 9).[99–105,108,109] In DUV LEDs, the poor p-type doping efficiency of high-Al-content AlGaN active regions has long been a major bottleneck limiting internal and external quantum efficiencies (IQE and EQE).[115] Low hole injection efficiency and high resistivity in p-type layers result in high turn-on voltages, large series resistance, severe self-heating, and reduced optical output power. The application of p-type modulation doping in AlGaN/GaN superlattices can effectively enhance the hole concentration and mobility in Al-rich AlGaN, thereby improving the conductivity of p-type layers, facilitating hole injection into the active region, reducing series resistance and operating voltage, and ultimately improving overall device performance.[116–118]

Figure 10 compares the performance distribution of five representative studies across four dimensions: peak external quantum efficiency (EQE), turn-on voltage, optical output power, and efficiency droop stability. It clearly reveals

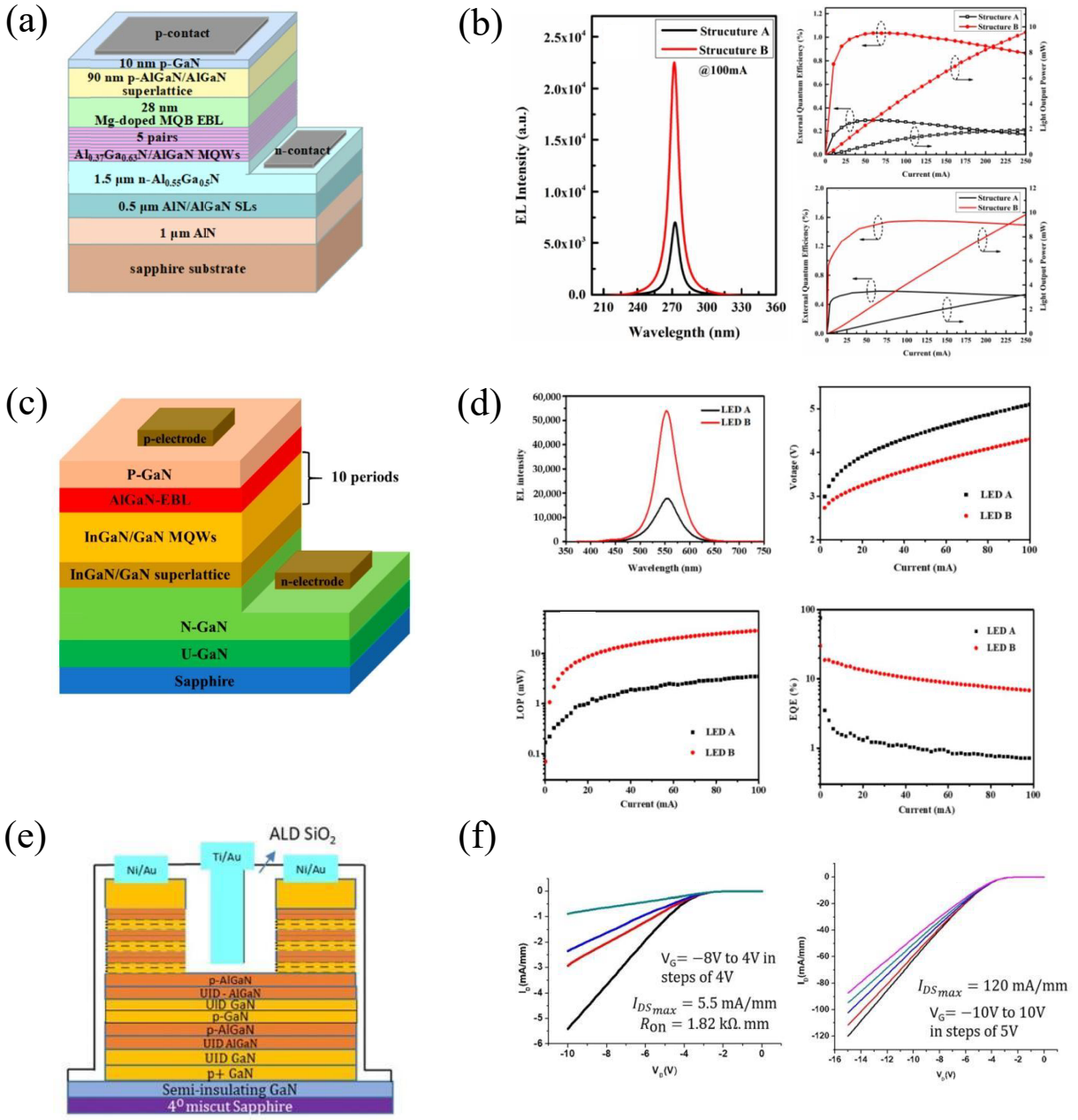


Fig. 9. Schematic structures and performance characteristics of AlGaN- and InGaN-based LEDs and N-polar AlGaN/GaN superlattice FETs. (a) and (b) Structures and electroluminescence characteristics of AlGaN-based deep-UV LEDs, showing single-peak emission and current-dependent EQE and LOP.[108] (c) and (d) Structures and optical performance of green–yellow InGaN/GaN LEDs, including EL spectra, voltage, LOP, and EQE as functions of injection current.[114] (e) and (f) Schematics and electrical characteristics of N-polar AlGaN/GaN superlattice FETs, comparing planar and FinFET configurations.[106]

the trade-offs between different technical routes and the core bottlenecks yet to be overcome in the DUV LED field. Yao *et al.*[119] reduced the turn-on voltage to a minimum of approximately 9 V through a polarization-enhanced superlattice structure; however, their EQE remains limited to about 2%, with an optical output power below 5 mW and mediocre droop control. This reflects the fundamental constraints in material quality and light extraction within the UVC band. The device by Wang *et al.*[116] presents the most balanced profile, achieving an EQE of 4%–5% — the highest among the DUV devices — and an optical output power of approximately 15 mW. Nevertheless, the reciprocal of their efficiency droop is only about 1.5–2.0, indicating that maintaining efficiency under high current density remains a significant weakness. Gu *et al.*[115] opted for an extreme technical route; while they achieved the best efficiency droop control, it came at the cost of a turn-on voltage skyrocketing to approximately 40 V and near-zero optical power. This suggests that the use of extremely thick electron-blocking structures effectively suppressed carrier overflow but severely sacrificed electrical injection efficiency — a classic trade-off between electrical performance and optical stability. The visible-light LED by Zhao *et al.*[89] serves as a reference group, naturally outperforming all DUV devices in EQE and output power. However, it shows no sig-

nificant advantage in turn-on voltage or efficiency droop, illustrating that even mature visible-light technology still has room for improvement. Wang *et al.*[113] occupy a unique niche. Their device achieved an EQE of approximately 4% and an optical output power of about 20 mW. With a turn-on voltage of 7–8 V and a superior efficiency droop reciprocal of about 3.0, their results validate that optimizing the superlattice period thickness to the 1 nm scale allows for an optimal balance between electrical injection, optical output, and high-current stability.

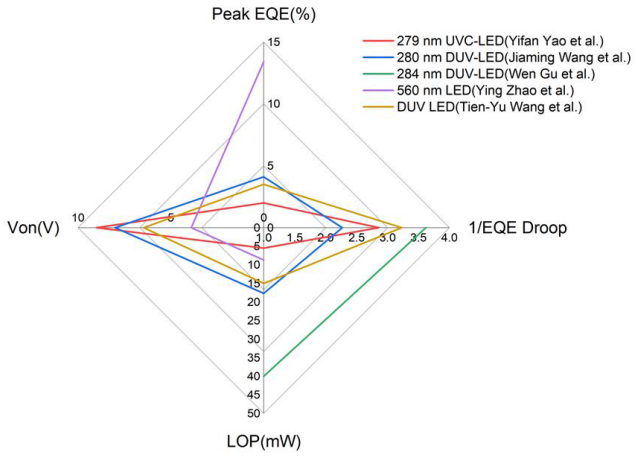


Fig. 10. Radar chart analysis of key performance metrics for LEDs with modulation-doped p-type AlGaN superlattices.[89,113,115,116,119]

Based on the research by Yao *et al.*,[119] the performance of 279 nm UVC LEDs is systematically governed by the composition contrast, period thickness, total thickness, and Mg-doping concentration of polarization-enhanced p-AlGaN superlattices (SLs). Their findings reveal that increasing the p-high/p-low Al-composition contrast from 60%/40% to 80%/20% triggers a 30-fold increase in hole concentration (from 7×10^{17} cm^{-3} to 2×10^{19} cm^{-3}), driving the external quantum efficiency (EQE) from $< 0.01\%$ to 1.5%. However, further increasing the contrast to 95%/5% causes the EQE to drop to 1.4% due to deteriorating interface roughness (RMS increasing from $<$ 1 nm to 3 nm) and increased parasitic absorption. This identifies a 60% composition contrast as the critical balance point between ionization efficiency and structural quality. Furthermore, while EQE remains relatively stable (1.4%–1.6%) for period thicknesses between 1.34 and 3.4 nm, it plummets by 65% (at 80 nm) once the total thickness exceeds 40 nm due to strain accumulation and light absorption. Mg-doping also exhibits a strict upper limit: EQE peaks at 1.5% with a concentration of 4×10^{19} cm^{-3}, but drops to 0.2% at 8×10^{19} cm^{-3} due to the formation of defects such as inversion domains. This underscores that polarization engineering is superior to heavy chemical doping alone. Complementary research by Wang *et al.*[113] on p-Al$*$0.8Ga$*$0.2N/Al$*$0.48Ga$*$0.52N SLs elucidates the coupling effect between period thickness and electro-optical performance. With a fixed total thickness of 20 nm, reducing the period from 4 nm to 2 nm lowers the forward voltage from 6.73 V to 6.46 V, boosts optical power by 15% (EQE: 2.58% to 3.15%), and improves efficiency droop from 37% to 31%. However, a further reduction to 1.32 nm weakens lateral current spreading, causing the power gain to regress to 4.3% and droop to rise back to 34%. This provides quantitative evidence of the inherent trade-off in the anisotropic conductivity of superlattices: shorter periods enhance longitudinal tunneling at the expense of lateral current spreading, with a 1 nm/1 nm ratio serving as the optimal balance. Additionally, the SL structure exhibits significantly higher transmittance in the 250–280 nm range compared to bulk materials, directly enhancing the light extraction efficiency (LEE). (Fig. 11)

Synthesizing these quantitative laws, the design of p-AlGaN superlattices must navigate multiple competing constraints:

(1) Composition contrast: Should be maintained within the 50%–70% window (optimally around 60%). This provides sufficient polarization fields to reach a hole concentration of $\sim 2 \times 10^{19}$ cm^{-3} while avoiding interface degradation and optical loss.

(2) Aluminum content (p-low layer): Should not fall below 20% to prevent 10%–30% parasitic absorption in the 260–280 nm target band.

(3) Dimensions: Individual layer thickness should range from 0.67 to 1.0 nm, with the number of periods maintained between 20 and 30 pairs.

(4) Total thickness: Must be strictly limited to under 40 nm to balance the tension between longitudinal tunneling, lateral current spreading, and strain accumulation.

Beyond DUV LEDs, p-type modulation-doped AlGaN also holds promise for III-nitride CMOS logic circuits and p-channel high-electron-mobility transistors (p-HEMTs).[106,107,110–112] Achieving high-performance p-channel devices is crucial for constructing GaN-based CMOS circuits and realizing low-power logic applications. The high-mobility 2DHG provided by p-type modulation doping offers an ideal channel material for p-channel field-effect transistors (pFETs).[106] Krishna *et al.*[107] implemented nitrogen-polar p-type GaN/AlGaN superlattices in wide-bandgap p-FETs, achieving a maximum drain current ($I_{\mathrm{DS,max}}$) exceeding 100 mA/mm — nearly 20$\times$ higher than that of planar devices — confirming the suitability of N-polar GaN/AlGaN SLs for high-performance p-FETs. Raj *et al.*[112] demonstrated an enhancement-mode (E-mode) p-channel MESFinFET based on GaN/AlGaN SLs, achieving an on-current (I_{on}) of 66 mA/mm, threshold voltage (V_{th}) of -0.6 V, and an on/off ratio exceeding 10^7. The depletion-mode (D-mode) device with 115-nm fin width achieved $I_{\mathrm{on}} = 78$ mA/mm, $V_{\mathrm{th}} = 1.2$ V, and an on/off ratio around 10^4.

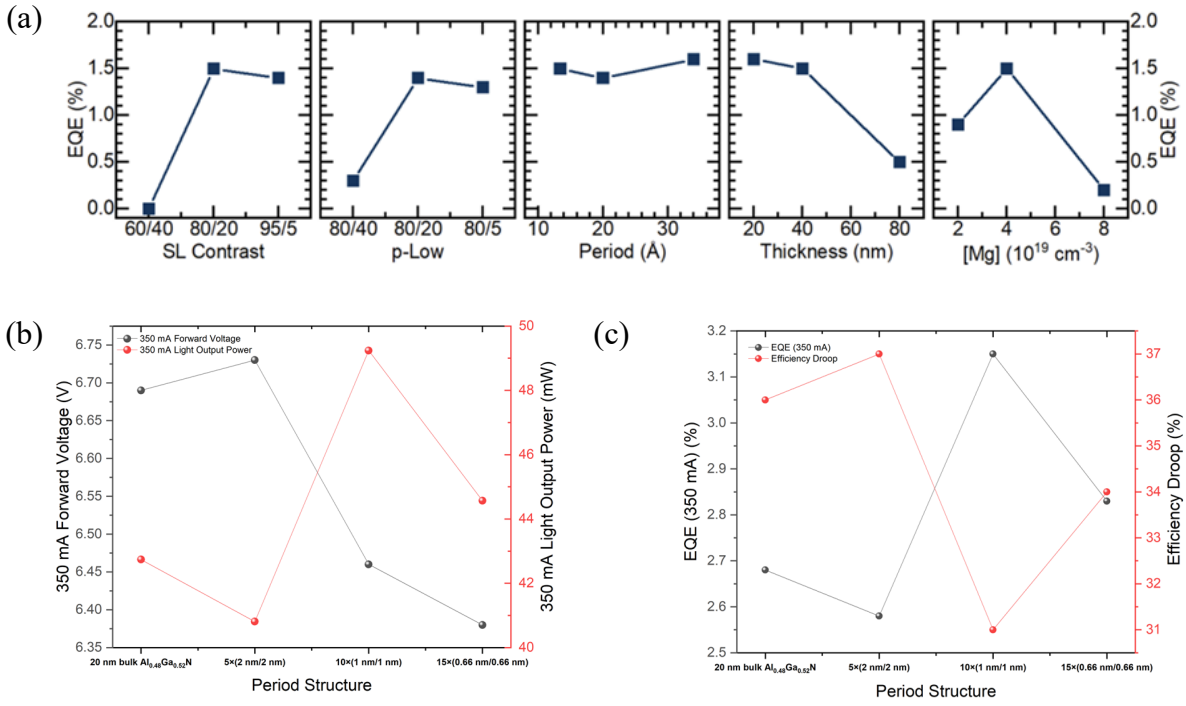


Fig. 11. Effects of p-type AlGaN superlattice design parameters on the performance of deep-ultraviolet LEDs. (a) External quantum efficiency (EQE) dependence on superlattice parameters: composition contrast, p-low Al content, period thickness, total thickness, and Mg-doping concentration.[119] (b)–(c) Forward voltage, light output power, EQE, and efficiency droop characteristics for different superlattice period structures at 350 mA.[113]

5.2. Diamond δ-doping and doping superlattices

Diamond, as a wide-bandgap semiconductor with exceptional physical and chemical properties, has become a highly promising material for next-generation high-power, high-frequency electronic devices and quantum technologies.[3,120] Its outstanding attributes — including ultra-high carrier mobility, excellent breakdown voltage, unmatched thermal conductivity, and remarkable chemical stability — position diamond as a leading candidate for future electronic systems.[3] However, the practical implementation of diamond electronics has long been hindered by challenges in doping technology. The major difficulties lie in the absence of shallow donors for effective n-type conduction and the high activation energy of boron acceptors, approximately 0.37 eV, for p-type conduction.[3] Therefore, diamond currently faces the same dilemma as AlGaN materials, namely the trade-off between high carrier concentration and high mobility. In contrast to AlGaN, boron δ-doping (delta-doping) and p–i–p–i structures in diamond utilize the insulator–metal (Mott) transition that occurs under extremely high boron concentrations, leading to metallic-like conductivity.[121] In this configuration, an atomically or nanometer-thick, heavily doped boron layer forms a two-dimensional conductive sheet. Such δ-doped structures are designed to confine carriers within a very thin region while allowing the wavefunctions to extend into adjacent undoped or lightly doped regions, thus reducing ionized impurity scattering.[122–124] This concept aims to achieve high carrier density without compromising mobility.[121,125] In diamond, boron δ-doping specifically refers to the formation of nanometer-scale, heavily boron-doped layers to create a 2DHG, providing a pathway for the development of high-frequency diamond-based FETs and two-dimensional hole devices.[123]

To realize the atomic-scale precision required for boron δ-doping and p–i–p–i structures, researchers have primarily employed advanced chemical vapor deposition (CVD) techniques, particularly microwave plasma-assisted CVD (MPCVD).[126–128] In many studies, multiple δ -doped layers are grown to investigate the depth distribution of boron concentration and Hall mobility. This configuration can be regarded as a diamond p–i–p–i doping superlattice structure, in which multiple δ -layers are periodically introduced to enhance hole mobility. However, research on such diamond-based p–i–p–i superlattices remains challenging and inconclusive. Although boron δ-layers with ideal doping profiles have been successfully fabricated — as confirmed by secondary ion mass spectrometry (SIMS) and transmission electron microscopy (TEM) — the experimentally observed hole mobility is significantly lower than theoretical predictions and shows little improvement compared with uniformly doped samples of similar average boron concentration.[122–124,129–133] Figure 12 summarizes the current progress in the investigation of the electrical properties of diamond doping superlattices, focusing on the optimization of two key parameters: the δ-layer thickness and the steepness of the dopant concentration profile at the interface. Theoretical analyses indicate that the

thickness of the δ-doped region must be significantly smaller than the de Broglie wavelength of holes in diamond (approximately 10 nm).[132] In addition, the boron concentration profile should exhibit a highly localized δ-function-like distribution along the growth direction. The characteristic length of the concentration transition region should also be shorter than the Debye length in diamond in order to enable the formation of a 2DHG.[124] At present, most reported δ-doped layers have thicknesses in the range of approximately 1–2.5 nm, which is considered one of the key requirements for achieving high-mobility diamond doping superlattices.[129–133] Considerable research efforts have therefore focused on achieving highly abrupt doping interfaces. As a result, the steepness of the dopant concentration profile has been improved to approximately 0.5–1.5 nm/dec.[129,130,132,133] However, these results are primarily obtained through interface etching techniques. For the growth of multi-period doping superlattice structures, such etching-based approaches are generally impractical.

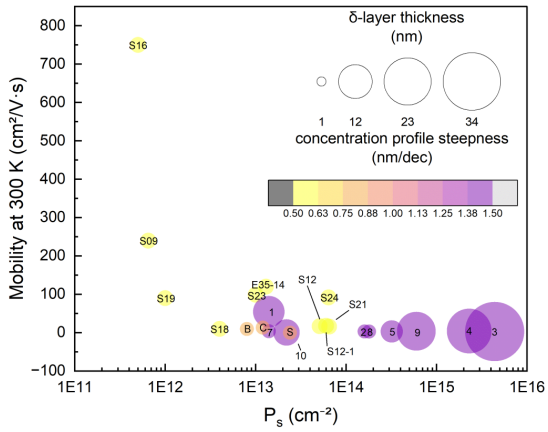


Fig. 12. Carrier mobility at 300 K as a function of sheet carrier density P_s for various δ-doped semiconductor structures. Bubble size represents the δ-layer thickness, while the color scale indicates the steepness of the dopant concentration profile. Samples 1–5 and 7–10 correspond to data reported in Refs. [130,133]. Samples S16, S19, S18, S09, S21, S23, E35-14, S24, S12, and S12-1 correspond to data reported in Ref. [129]. Samples B, C, and S correspond to data reported in Ref. [132].

Recent theoretical analyses suggest that earlier models may have underestimated the confinement potential of holes within δ-doped layers.[121] At extremely high boron concentrations ($\sim 10^{21}$ cm^{-3}), the strong Coulomb potential of ionized boron atoms leads to a significant downward shift of the valence band edge, producing a deeper quantum well than previously anticipated. This enhanced confinement suppresses the spatial extension of hole wavefunctions into adjacent intrinsic regions, thereby weakening the intended reduction in impurity scattering. Theoretical models predict that achieving a substantial mobility improvement would require metallic δ-layers thinner than 0.5 nm with compensation ratios below approximately 42%.[121,122,133] However, fabricating such ultra-thin, high-quality, and heavily doped layers remains experimentally formidable due to growth kinetics and surface stability constraints. Apart from the confinement and doping effects, several extrinsic factors further limit hole mobility in δ-doped diamond structures and p–i–p–i structures. The most critical among these is interface quality. Ideally, δ-doped layers should possess atomically sharp and smooth interfaces between the doped and intrinsic regions. In practice, finite gas-switching response times, boron surface diffusion, and minor substrate irregularities frequently lead to interface broadening or roughness.[122,126–128,134] Another major limiting factor is the presence of crystal defects, which act as scattering centers and carrier traps. These traps can significantly reduce the effective carrier concentration and, consequently, the measured Hall mobility. Experiments have revealed a marked discrepancy between the boron atomic sheet density (N_{2D}) and the hole sheet density (P_s) derived from Hall measurements — where N_{2D} values typically reach $(14.3–19.9)\times10^{13}$ cm^{-2}, while P_s can be several orders of magnitude lower. This inconsistency is generally attributed to incomplete ionization of boron atoms or the existence of deep-level traps within or near the δ-doped regions.[122]

6. Summary and outlook

Doping superlattices (DSLs) and δ-doping techniques have evolved into a versatile platform for precise control of carrier distribution, band structure, and optoelectronic behavior in both conventional and wide-bandgap semiconductor materials. Through the rational design of layer periodicity, doping concentration, and heterointerface band alignment, DSL architectures — particularly n–i–p–i, n–p–n–p, and n–i–n–i configurations — enable spatial separation of carriers and tunable subband structures, leading to long carrier lifetimes, reduced recombination rates, and adjustable optical responses. These unique features have given rise to a broad range of device applications, including high-efficiency solar cells, infrared photodetectors, electro-optic modulators, and negative-differential-resistance transistors. The combination of optical and electrical tunability within DSLs has demonstrated substantial potential for high-speed and radiation-resistant optoelectronic systems, as confirmed by numerous GaAs- and GaInNAs-based prototypes. Moreover, δ-doped and sawtooth superlattice configurations have proven highly effective in achieving large electroabsorption modulation, tunable luminescence, and broadband photoconductive gain, confirming that doping-superlattice engineering represents a general physical framework for achieving simultaneously high mobility, high gain, and spectral tunability.

In WBG materials such as AlGaN and diamond, these doping-superlattice concepts have been successfully extended to overcome fundamental doping limitations. In AlGaN, the high activation energy of Mg acceptors restricts hole generation, leading to low conductivity and poor efficiency in DUV

emitters. By employing short-period superlattices or δ-doped barrier layers, the ionization energy of Mg can be effectively reduced through polarization-induced band bending, enabling hole transfer into adjacent GaN wells and thereby improving p-type conductivity and injection efficiency. This mechanism mirrors the modulation-doping principle in III–V heterostructures, providing enhanced hole mobility and reduced compensation in Al-rich AlGaN. As a result, p-type modulation-doped AlGaN superlattices have demonstrated significant performance improvements in DUV LEDs, p-channel HEMTs, and CMOS logic devices.

For diamond, boron δ-doping and p–i–p–i doping superlattices offer an analogous strategy to form 2DHGs with high carrier density and mobility. These approaches exploit the Mott transition and the unique potential profile of ultra-thin, heavily boron-doped layers to spatially decouple holes from ionized impurities. However, despite substantial theoretical progress, experimental realizations still face major challenges — particularly in achieving atomically abrupt interfaces, minimizing boron compensation, and maintaining crystal perfection. Addressing these issues requires advances in plasma-enhanced CVD growth, in-situ surface control, and nanoscale dopant characterization.

Looking forward, future developments in diamond-based DSLs may extend beyond boron to address the long-standing difficulty of realizing stable n-type conduction. The n–i–n–i superlattice architecture, analogous to the n–i–p–i system but composed solely of donor-doped and intrinsic layers, could provide a promising route to mitigate the deep donor activation energy of phosphorus in diamond. By engineering alternating heavily phosphorus-doped (n) and intrinsic (i) layers, the built-in electrostatic potential could facilitate field-assisted donor ionization and spatial confinement of electrons in potential wells, effectively forming a quasi-2DEG. Such structures may reduce the effective activation energy of phosphorus donors through band-edge modulation and quantum confinement, while preserving high electron mobility by separating free carriers from ionized centers. Coupled with optimized hydrogen termination, strain control, and interface passivation, the n–i–n–i concept offers a feasible pathway toward achieving n-type diamond with practical conductivity — potentially enabling all-diamond pn junctions, high-frequency transistors, and radiation-hard electronic platforms.

In summary, doping-superlattice engineering provides a unifying physical and technological foundation for achieving high-mobility, high-efficiency, and tunable semiconductor devices across both narrow- and wide-bandgap material systems. For AlGaN, it effectively lowers acceptor activation energies and enhances p-type transport; for diamond, it opens new opportunities to overcome the bottlenecks of both p- and n-type doping. Continued interdisciplinary progress — spanning epitaxial growth, first-principles theory, and device integration — will be crucial to translating these advances from fundamental research to scalable, next-generation optoelectronic and power-electronic technologies.

Acknowledgments

Project supported by the National Key R&D Program of China (Grant No. 2024YFE0205200) and the National Natural Science Foundation of China (Grant Nos. 62274084 and 62574106).

References

[1] Chen Y X, Ben J W, Xu F J, Li J C, Chen Y, Sun X J and Li D B 2021 *Fundam. Res.* **1** 717
[2] Tsao J Y, Chowdhury S, Hollis M A, *et al.* 2018 *Adv. Electron. Mater.* **4** 1600501
[3] Filippatos P P and Chroneos A 2025 *J. Appl. Phys.* **138** 030702
[4] Döhler G H 1986 *Crit. Rev. Solid State Mater. Sci.* **13** 97
[5] Döhler G 1986 *IEEE J. Quantum Electron.* **22** 1682
[6] Schubert E F, Grieshaber W and Goepfert I D 1996 *Appl. Phys. Lett.* **69** 3737
[7] Denisenko A and Kohn E 2005 *Diam. Relat. Mater.* **14** 491
[8] Peng R Q, Su W K, Yu Z G, Cao J M, Jiang D W, Wang D B and Jiao S J 2024 *Nanomaterials* **14** 682
[9] Muhammetgulyyev A, Yalcin Y, Kuruoglu F, Cokduygulular E, Kinaci B and Erol A 2021 *Opt. Quantum Electron.* **53** 29
[10] Muhammetgulyyev A, Kinaci B, Aho A, Yalcin Y, Cetinkaya C, Kuruoglu F, Guina M and Erol A 2018 *Appl. Phys. A* **125** 27
[11] Vaghjiani H L, Johnson E A, Kane M J, Grey R and Phillips C C 1994 *J. Appl. Phys.* **76** 4407
[12] Maserjian J, Grunthaner F J and Elliott C T 1990 *Infrared Phys.* **30** 27
[13] Hass K C and Kirill D J 1990 *J. Appl. Phys.* **68** 1923
[14] Tan C M, Xu J M and Zukotynski S 1993 *J. Appl. Phys.* **73** 2921
[15] Goepfert I D, Schubert E F, Osinsky A and Norris P E 1999 *Electron. Lett.* **35** 1109
[16] Hsu L and Walukiewicz W 1999 *Appl. Phys. Lett.* **74** 2405
[17] Tribuzy C V B, Areiza M C L, Landi S M, Borgstrom M, Pires M P and Souza P L 2005 *Appl. Phys. Lett.* **86** 023501
[18] Areiza M, Tribuzy C, Landi S, Pires M and Souza P 2005 *IEEE Photonics Technol. Lett.* **17** 2071
[19] Tribuzy C V B, Pires M P and Souza P L 2004 *Microw. Opt. Technol. Lett.* **43** 168
[20] Dutta N, Choudhury N, Zhu G and Cong H 2003 *Modulation-Doped InGaAsP Quantum Well Laser and Modulator*, September 08–11, 2003, ORLANDO, FL, p. 275
[21] Choudhury N and Dutta N K 2001 *J. Appl. Phys.* **90** 38
[22] Ruden P and Döhler G H 1983 *Phys. Rev. B* **27** 3538
[23] Renn M, Metzner C and Döhler G H 1993 *Phys. Rev. B* **48** 11220
[24] Döhler G H 1983 *J. Vac. Sci. Technol. B* **1** 278
[25] Ploog K, Kunzel H, Knecht J, Fischer A and Döhler G H 1981 *Appl. Phys. Lett.* **38** 870
[26] Kunzel H, Döhler G H and Ploog K 1982 *Appl. Phys. A* **27** 1
[27] Döhler G H, Kunzel H and Ploog K 1982 *Phys. Rev. B* **25** 2616
[28] Döhler G H and Ruden P R 1984 *Phys. Rev. B* **30** 5932
[29] Hasnain G, Changhasnain C J, Döhler G H, Miller J N, Johnson N M, Whinnery J R and Dienes A 1987 *Superlattices Microstruct.* **3** 277
[30] Linder N, Schmidt K H, Geisselbrecht W, Döhler G H, Grahn H T, Ploog K and Schneider H 1995 *Phys. Rev. B* **52** 17352
[31] Malzer S, Linder N, Gulden K H, Hofler A, Kiesel P, Kneissl M, Wu X, Smith J and Döhler G H 1992 *Phys. Status Solidi B* **173** 459
[32] Döhler G H, Fasol G, Low T S, Miller J N and Ploog K 1986 *Solid State Commun.* **57** 563
[33] Beyer H J, Metzner C, Heitzer J and Döhler G H 1989 *Superlattices Microstruct.* **6** 351
[34] Cress C D, Polly S J, Hubbard S M, Raffaelle R P and Walters R J 2011 *Prog. Photovoltaics* **19** 552
[35] Street R A, Döhler G H, Miller J N and Ruden P P 1986 *Phys. Rev. B* **33** 7043

[36] Jung H, Döhler G H, Gobel E O and Ploog K 1983 *Appl. Phys. Lett.* **43** 40

[37] Freundlich A, Slocum M A, Forbes D V, Hubbard S M and Guillemoles J F 2012 *Interface Quality Enhancement of the Epitaxial Regrowth Process for Nipi Photovoltaic Devices*, January 23–26, 2012, San Francisco, CA, p. 82561B

[38] Slocum M A, Forbes D V and Hubbard S M 2014 *Enhancement of Radiation Tolerance with the Use of a Doping Superlattice Solar Cell*, 2014, San Francisco, CA, p. 89810V

[39] Yagi S, Noguchi S, Hijikata Y, Kuboya S, Onabe K, Okada Y and Yaguchi H 2013 *Optical Absorption by E_+ Miniband of GaAs:Nδ-Doped Superlattices*, June 16–21, 2013, Tampa, FL, p. 2490

[40] Yakes M K, Cress C D, Lumb M P, Warner J H, Bailey C G, Hoheisel R and Walters R J 2012 *Bandgap Engineering Achieved with Doping Superlattices*, June 03–08, 2012, Austin, TX, p. 2979

[41] Mazzucato S, Royall B, Ketlhwaafetse R, Balkan N, Salmi J, Puustinen J, Guina M, Smith A and Gwilliam R 2012 *Nanoscale Res. Lett.* **7** 631

[42] Slocum M A, Forbes D V and Hubbard S M 2015 *Modeling nipi Solar Cells under Concentration Accounting for State Filling Effects*, February 10–12, 2015, San Francisco, CA, p. 93580K

[43] Slocum M A 2015 *Development and Characterization of a GaAs nipi Superlattice Solar Cell* (Ph.D. Dissertation) (Rochester Institute of Technology)

[44] Slocum M A, Forbes D V, Grede A J, Hoven N M and Hubbard S M 2014 *Improving Epitaxial Regrowth Interfaces as a Means of Improving Doping Superlattice Solar Cell Performance*, June 08–13, 2014, Denver, CO, pp. 102

[45] Koehler S D, Garmire E M, Kost A R, Yap D, Docter D P and Hasenberg T C 1995 *IEEE Photonics Technol. Lett.* **7** 878

[46] Kiesel P, Kneissl M, Riel P, Reingruber K, Gulden K, Greger E, Knupfer B, Wu X, Smith J and Döhler G H 1995 *Dynamical Behavior of Optooptical Logic Switching Devices Employing N-I-P-I-Based Smart Pixels*, August 22–25, 1994, Heriot-Watt Univ., Edinburgh Conf Ctr, Edinburgh, Scotland, pp. 573

[47] Osipov V, Selyakov A and Foygel M 1998 *Phys. Status Solidi A* **169** 161

[48] Phillips C C 1990 *Appl. Phys. Lett.* **56** 151

[49] Riel P, Kiesel P, Ennes M, Gabler T, Kneissl M, Bohm G, Trankle G, Weimann G, Gulden K H, Wu X X, Smith J S and Döhler G H 1992 *n-i-p-i-BASED High-Speed Detectors And Bistable Switches With Gain*, March 23–24, 1992, Somerset, NJ, pp. 242

[50] Kiesel P, Riel P, Lin H, Linder N, Miller J F and Döhler G H 1989 *Superlattices Microstruct.* **6** 363

[51] Ackley D E, Mantz J, Lee H, Nouri N and Shieh C L 1988 *Appl. Phys. Lett.* **53** 125

[52] Schubert E, Fischer A and Ploog K 1985 *Electron. Lett.* **21** 411

[53] Schubert E F, Fischer A, Horikoshi Y and Ploog K 1985 *Appl. Phys. Lett.* **47** 219

[54] Vojak B A, Zajac G W, Chambers F A, Meese J M, Chumbley P E, Kaliski R W, Holonyak N and Nam D W 1986 *Appl. Phys. Lett.* **48** 251

[55] Liu W C, Sun C Y, Hsu W C and Guo D F 1993 *Jpn. J. Appl. Phys.* **32** 1575

[56] Sun C Y and Liu W C 1992 *Solid-State Electron.* **35** 751

[57] Su Y K, Wang R L and Tsai H H 1993 *IEEE Trans. Electron Devices* **40** 2192

[58] Sun C Y and Liu W C 1991 *Appl. Phys. Lett.* **59** 2823

[59] Kiesel P, Gulden K H, Hofler A, Kneissl M, Knupfer B, Linder N, Riel P, Wu X, Smith J S and Döhler G H 1993 *Superlattices Microstruct.* **13** 21

[60] Thirstrup C, Robson P N, Kam Wa P L, Pate M A, Button C C and Roberts J S 1994 *J. Lightwave Technol.* **12** 425

[61] Larsson A and Maserjian J 1991 *Appl. Phys. Lett.* **59** 3099

[62] Larsson A G and Maserjian J 1992 *Opt. Eng.* **31** 1576

[63] Yoffe G W, Brubach J, Karouta F, Van Der Vleuten W C, Kaufmann L M F and Wolter J H 1993 *Appl. Phys. Lett.* **63** 1456

[64] Tribuzy C V B, Butendeich R, Pires M P, Souza P L and Henriques A B 2001 *J. Appl. Phys.* **90** 1660

[65] Tribuzy C V B, Pires M, Landi S, Borgstrom M and Souza P 2004 *Appl. Phys. Lett.* **84** 3256

[66] Knupfer B, Kiesel P, Hofler A, Riel P, Döhler G H and Veuhoff E 1993 *Appl. Phys. Lett.* **62** 2072

[67] Kiesel P, Gulden K H, Hofler A, Kneissl M, Knupfer B, Dankowski S, Riel P, Wu X, Smith J S, Weimann G and Döhler G H 1993 *Optical Bistability Of p-i-n and n-i-p-i Structures at Very-Low Optical Power*, May 24–27, 1993, Trieste, Italy, pp. 278

[68] Li M Z, Zhang M L, Ji X Q, Li S, Yang L L and Tang W H 2026 *Chin. Phys. B* **35** 028502

[69] Wang J M, Xu F J, Zhang L S, Lang J, Fang X Z, Zhang Z Y, Guo X Q, Ji C, Ji C Z, Tan F Y, Yang X L, Kang X N, Qin Z X, Tang N, Wang X Q, Ge W K and Shen B 2024 *J. Semicond.* **45** 021501

[70] Nabila K T and Hudgins J L 2025 *A Physics-Based Temperature Dependent Analytical Model For 2DEG Density in AlGaN/GaN HEMT Devices*, March 16–20, 2025, Atlanta, GA, p. 2877

[71] Waldron E, Graff J and Schubert E 2001 *Appl. Phys. Lett.* **79** 2737

[72] Kumakura K and Kobayashi N 1999 *Jpn. J. Appl. Phys.* **38** L1012

[73] Saxler A, Mitchel W C, Kung P and Razeghi M 1999 *Appl. Phys. Lett.* **74** 2023

[74] Goepfert I D, Schubert E F, Osinsky A, Norris P E and Faleev N N 2000 *J. Appl. Phys.* **88** 2030

[75] Kozodoy P, Xing H L, Denbaars S P, Mishra U K, Saxler A, Perrin R, Elhamri S and Mitchel W C 2000 *J. Appl. Phys.* **87** 1832

[76] Kumakura K, Makimoto T and Kobayashi N 2000 *Jpn. J. Appl. Phys.* **39** 2428

[77] Kumakura K, Makimoto T and Kobayashi N 2000 *Jpn. J. Appl. Phys.* **39** L195

[78] Polyakov A Y, Smirnov N B, Govorkov A V, Osinsky A V, Norris P E, Pearton S J, Van Hove J, Wowchack A M and Chow R R 2001 *J. Appl. Phys.* **90** 4032

[79] Waldron E L, Graff J W and Schubert E F 2001 *Appl. Phys. Lett.* **79** 2737

[80] Kim J K, Waldron E L, Li Y L, Gessmann T, Schubert E F, Jang H W and Lee J L 2004 *Appl. Phys. Lett.* **84** 3310

[81] Hertkorn J, Bruckner P, Gao C, Scholz F, Chuvilin A, Kaiser U, Wurstbauer U and Wegscheider W 2008 *Transport properties in n-type AlGaN/AlN/GaN-superlattices*, September 16–21, 2007, Las Vegas, NV, p. 1950

[82] Namkoong G, Trybus E, Lee K K, Moseley M, Doolittle W A and Look D C 2008 *Appl. Phys. Lett.* **93** 172112

[83] Liu Z Q, Yi X Y, Yu Z G, Yuan G D, Liu Y, Wang J X, Li J M, Lu N, Ferguson I and Zhang Y 2016 *Sci. Rep.* **6** 19537

[84] Chen H T, Su C Y, Tu C G, Yao Y F, Lin C H, Wu Y R, Kiang Y W and Yang C C 2017 *IEEE Trans. Electron Devices* **64** 115

[85] Ebata K, Nishinaka J, Taniyasu Y and Kumakura K 2018 *Jpn. J. Appl. Phys.* **57** 04FH09

[86] Chen C C, Lin Y R, Lin Y W, Su Y C, Chen C C, Huang T C, Wu P H, Yang C C, Mou S and Averett K L 2021 *Micromachines* **12** 835

[87] Wang L, Li R, Li D, Liu N Y, Liu L, Chen W H, Wang C D, Yang Z J and Hu X O 2010 *Appl. Phys. Lett.* **96** 061110

[88] Liu N, Li D, Wang L, Liu L, Yang W, Li L, Cao W Y, Lu C M, Wan C H, Chen W H and Hu X D 2012 *Jpn. J. Appl. Phys.* **51** 071001

[89] Zhao Y, Xu S R, Tao H C, Zhang Y C, Zhang C F, Feng L S, Peng R S, Fan X M, Du J J, Zhang J C and Hao Y 2021 *Materials* **14** 144

[90] Fan A, Zhang X, Chen S, Li C, Lu L, Zhuang Z, Lyu J D, Hu G H and Cui Y P 2020 *Superlattices Microstruct.* **145** 106632

[91] Zheng T C, Lin W, Liu R, Cai D J, Li J C, Li S P and Kang J Y 2016 *Sci. Rep.* **6** 21897

[92] Bennett S E, Ulfig R M, Clifton P H, Kappers M J, Barnard J S, Humphreys C J and Oliver R A 2011 *Ultramicroscopy* **111** 207

[93] Yao Y F, Chen H T, Kuo Y, Su C Y, Tu C G, Lin C H, Kiang Y W and Yang C C 2018 *Superlattices Microstruct.* **124** 107

[94] Kozodoy P, Smorchkova Y P, Hansen M, Xing H, Denbaars S P, Mishra U K, Saxler A W, Perrin R and Mitchel W C 1999 *Appl. Phys. Lett.* **75** 2444

[95] Liu X L, Yuan H R, Lu D C and Wang X H 2000 *Modulation Magnesium-Doping in AlGaN/GaN Superlattices*, September 24–27, 2000, Nagoya, Japan, pp. 732

[96] Hackenbuchner S, Majewski J A, Zandler G and Vogl P 2001 *J. Cryst. Growth* **230** 607

[97] Li J C and Kang J Y 2007 *Appl. Phys. Lett.* **91** 152106

[98] Zheng Q H, Yin Y A, Zhu L H, Huang J, Li X Y and Liu B L 2009 *Appl. Phys. Lett.* **94** 222104

[99] Singh C P and Ghosh K 2025 *Mater. Sci. Eng. B* **322** 118601

[100] Li J, Yang W H, Li S P, Chen H Y, Liu D Y and Kang J Y 2009 *Appl. Phys. Lett.* **95** 151113

[101] Allerman A A, Crawford M H, Miller M A and Lee S R 2010 *J. Cryst. Growth* **312** 756

[102] Cheng B, Choi S, Northrup J E, Yang Z, Knollenberg C, Teepe M, Wunderer T, Chua C L and Johnson N M 2013 *Appl. Phys. Lett.* **102** 231106

[103] Song H, Jeon K S, Joe J H, Kim S, Lee M, Lee E A, Choi H, Sung J, Kang M G, Choi Y H and Lee J S 2013 *Appl. Phys. Lett.* **103** 141102

[104] Maeda N, Jo M and Hirayama H 2018 *Phys. Status Solidi A* **215** 1700436

[105] Mehta K, Liu Y S, Wang J, Jeong H, Detchprohm T, Park Y J, Alugubelli S R, Wang S, Ponce F A, Shen S C, Dupuis R D and Yoder P D 2018 *IEEE J. Quantum Electron.* **54** 1

[106] Krishna A, Raj A, Hatui N, Koksaldi O, Jang R, Keller S and Mishra U K 2019 *Phys. Status Solidi A* **217** 1900692

[107] Krishna A, Raj A, Hatui N, Keller S and Mishra U K 2019 *Appl. Phys. Lett.* **115** 172105

[108] Lang J, Xu F J, Ge W K, Liu B Y, Zhang N, Sun Y H, Wang J M, Wang M X, Xie N, Fang X Z, Kang X N, Qin Z X, Yang X L, Wang X Q and Shen B 2019 *Opt. Express* **27** A1458

[109] Sato K, Yasue S, Ogino Y, Iwaya M, Takeuchi T, Kamiyama S and Akasaki I 2019 *Jpn. J. Appl. Phys.* **58** 1016

[110] Krishna A, Raj A, Hatui N, Koksaldi O, Jang R, Keller S and Mishra U K 2020 *Phys. Status Solidi A* **217** 1900692

[111] Raj A, Krishna A, Hatui N, Gupta C, Jang R, Keller S and Mishra U K 2020 *IEEE Electron Device Lett.* **41** 220

[112] Raj A, Krishna A, Hatui N, Romanczyk B, Wurm C, Guidry M, Hamwey R, Pakala N, Keller S and Mishra U K 2021 *GaN/AlGaN Superlattice Based E-Mode P-Channel Mes-Finfet with Regrown Contacts and* $>$ 50 *Ma/Mm On-Current*, December 11–16, 2021, San Francisco, CA, pp. 110

[113] Wang T Y, Lai W C, Sie S Y, Chang S P, Kuo C H and Sheu J K 2021 *Processes* **9** 1727

[114] Zhao Y, Xu S R, Tao H C, Zhang Y C, Zhang C F, Feng L S, Peng R S, Fan X M, Du J J, Zhang J C and Hao Y 2021 *Materials* **14** 144

[115] Gu W, Lu Y, Liu Z Y, Liao C H, Yan J C, Wang J X, Li J M and Li X H 2022 *Micro Nanostructures* **163** 107128

[116] Wang J M, Wang M X, Xu F J, Liu B Y, Lang J, Zhang N, Kang X N, Qin Z X, Yang X L, Wang X Q, Ge W K and Shen B 2022 *Light Sci. Appl.* **11** 71

[117] Du J J, Cheng H C, Li Y, Chen P, Zhang R Y, Guo X, Zhu Y F, Miao Z, Zhang Y J and Liu L 2023 *AIP Adv.* **13** 095301

[118] Tao H C, Xu S R, Zhang Y C, Su H K, Gao Y, Liu X, Ding R X, Xie L, Wang H T, Zhang J C and Hao Y 2024 *Fundam. Res.* **6** 155

[119] Yao Y, Zollner C J, Wang M, Iza M, Speck J S and Denbaars S P 2022 *IEEE J. Quantum Electron.* **58** 1

[120] Ichikawa K, Matsumoto T, Inokuma T, Yamasaki S, Nebel C E and Tokuda N 2024 *Acc. Mater. Res.* **5** 1181

[121] Kukushkin V A 2022 *Semiconductors* **56** 742

[122] Lobaev M A, Vikharev A L, Gorbachev A M, Radishev D B, Arkhipova E A, Drozdov M N, Isaev V A, Bogdanov S A and Kukushkin V A 2022 *Nanosyst. Phys. Chem. Math.* **13** 578

[123] Balmer R S, Friel I, Hepplestone S, Isberg J, Uren M J, Markham M L, Palmer N L, Pilkington J, Huggett P, Majdi S and Lang R 2013 *J. Appl. Phys.* **113** 033702

[124] El-Hajj H, Denisenko A, Bergmaier A, Dollinger G, Kubovic M and Kohn E 2008 *Diam. Relat. Mater.* **17** 409

[125] Kukushkin V A, Snider G, Bogdanov S A and Chernov V V 2014 *Phys. Status Solidi RRL* **8** 876

[126] Litvak A G, Vikharev A L, Gorbachev A M, Lobaev M A, Radishev D B, Isaev V A, Bogdanov S A, Drozdov M N, Demidov E V, Surovegina E A, Shashkin V I, Yunin P A and Butler J E 2017 *CVD Diamond with Boron-Doped Delta-Layers Deposited by Microwave Plasma*, July 17–22, 2017, Nizhny Novgorod, RUSSIA, pp. 1

[127] Vikharev A L, Gorbachev A M, Lobaev M A, Muchnikov A B, Radishev D B, Isaev V A, Chernov V V, Bogdanov S A, Drozdov M N and Butler J E 2016 *Phys. Status Solidi RRL* **10** 324

[128] Mer-Calfati C, Tranchant N, Volpe P, Arnault J, Bergonzo P and Jomard F 2014 *Diamond Delta Doped Structures Exhibiting Ultra-Sharp Interfaces*, October 06–07, 2014, Rome, ITALY, p. 144

[129] Butler J E, Vikharev A, Gorbachev A, Lobaev M, Muchnikov A, Radischev D, Isaev V, Chernov V, Bogdanov S, Drozdov M, Demidov E, Surovegina E, Shashkin V, Davydov A, Tan H, Meshi L, Pakpour-Tabrizi A C, Hicks M L and Jackman R B 2016 *Phys. Status Solidi RRL* **11** 1600329

[130] Chicot G, Fiori A, Volpe P N, *et al.* 2014 *J. Appl. Phys.* **116** 083702

[131] Scharpf J, Denisenko A, Pakes C I, Rubanov S, Bergmaier A, Dollinger G, Pietzka C and Kohn E 2013 *Phys. Status Solidi A* **210** 2028

[132] Edgington R, Sato S, Ishiyama Y, Morris R, Jackman R B and Kawarada H 2012 *J. Appl. Phys.* **111** 033710

[133] Chicot G, Tran Thi T N, Fiori A, Jomard F, Gheeraert E, Bustarret E and Pernot J 2012 *Appl. Phys. Lett.* **101** 162101

[134] Fiori A, Tran Thi T N, Chicot G, Jomard F, Omnes F, Gheeraert E and Bustarret E 2012 *Diam. Relat. Mater.* **24** 175